C. Paravan, L. Galfetti, R. Bisin, F. Piscaglia
Combustion Processes in Hybrid Rockets
International Journal of Energetic Materials and Chemical Propulsion, Vol. 18, N. 3, 2019, p. 255-286
doi:10.1615/IntJEnergeticMaterialsChemProp.2019027834

COMBUSTION PROCESSES IN HYBRID ROCKETS

Christian Paravan, Luciano Galfetti, Riccardo Bisin, and Federico Piscaglia

Politecnico di Milano
Aerospace Science and Technology Department, Space Propulsion Laboratory (SPLab)
34, via La Masa, 20156 Milano, Italy

christian.paravan@polimi.it

This paper presents the latest results achieved at the Space Propulsion Laboratory (SPLab) of Politecnico di Milano in the area of hybrid propulsion. Focus is put on four specific research topics, currently under investigation, and strongly linked: 1. solid fuel formulations development; 2. investigation of liquefying fuel formulations responsible for the entrainment phenomenon; 3. development of a vortex flow pancake (VFP) designed for in-space missions; 4. numerical simulation approaches. A wide chemical, thermal, rheological, mechanical and ballistic investigation of traditional polymeric formulations and paraffin-based solid fuels has been performed in the last years and is shortly summarized here. Firing tests are performed in a radial lab-scale burner enabling time-resolved regression rate measurements. The results of this activity pave the way to the challenging horizon of liquefying fuel formulations. The entrainment of melted fuels is investigated by a dedicated setup designed for the study of the oxidizer stream/melt surface interaction under cold-flow conditions, to understand the droplet formation mechanism and to measure their size distribution. The effects of liquid layer entrainment on the combustion processes seem attractive for the development of unusual geometries, such as the VFP. The VFP hybrid rocket configuration offers a compact implementation with motor length-to-diameter ratio lower than 1, giving a breakthrough opportunity for in-space missions that could strongly benefit from the system affordability, with low recurring costs joined to high operating flexibility. The VFP development requires a strong support of numerical simulation activities, developed through OpenFOAM, and described in the last part of the paper.

KEY WORDS: hybrid propulsion, solid fuels, liquefying solid fuels, entrainment phenomena, vortex flow pancake, regression rate, combustion efficiency

Nomenclature

LATIN SYMBOLS

Ci	circularity (for entrained melted fuel droplets)
D	diameter, mm
D_{10}	droplet average number diameter, $D_{10}=\sum_{i=1}^{n} D_i / \sum_{i=1}^{n} i$, µm
D_{32}	droplet average surface diameter, $D_{32}=\sum_{i=1}^{n} D_i^3 / \sum_{i=1}^{n} D_i^2$ µm
$D_{0.5}$	droplet size distribution median diameter, µm
g	rescaling function (see Sec. 7)
G	total mass flux (sum of fuel and oxidizer mass fluxes), kg/(m^{2}s)
G_f	fuel mass flux, kg/(m^{2}s)
G_{ox}	oxidizer mass flux, kg/(m^{2}s)
h	enthalpy, J/kg
H_{cc}	combustion chamber height, m
I_s	specific impulse, s
l_t	minimum integral length scale, mm
L	length, m
L_t	integral length scale, mm
$\dot{m}$	mass flow rate, kg/s
m	mass, kg
p	pressure, MPa
A_b	regression surface, m^2
A_t	nozzle throat area, m^2
c*	combustion chamber characteristic velocity, m/s
MW	molecular weight, kg/kmol
r_f	solid fuel regression rate, mm/s
$r_{f,\,Norm}$	normalized solid fuel regression rate, mm/s
T	temperature, K
t	time, s
t_{flow}	flowmeter response time, s
th	thickness, mm
V	volume, m^3
v	velocity, m/s
v_{ox}	oxidizer flow velocity, m/s
x	longitudinal coordinate, m

GREEK SYMBOLS

α	minimum number of grid points needed to resolve a turbulent structure
β	coefficient to limit the temporal resolution to resolve a turbulent structure
Δf	minimum resolvable length scale, mm
$\acute{\Delta}_l$	spatial resolution, mm
Δh_{sens}	distance between wires of a wire-cut sensor, mm

$\acute{\Delta}_{\tau}$	temporal resolution, s
Δh_{i-j}	distance between two consecutive wires (i-th, and j-th), mm
δ	characteristic heat diffusion thickness, defined as α/r_f , m
δ_t	time step size, s
η_{c^*}	c* efficiency, $c^*_{real}/c^*_{ideal,\ -}$
η_f	melt fuel dynamic viscosity, Pa s
ρ	density, kg/m^3
τ	characteristic heat diffusion time, $\alpha/r_f^{\ 2}$, s

ACRONYMS AND ABBREVIATIONS

CB	Carbon Black
CEA	Chemical Equilibrium with Applications
DOA	Di-Octyl Adipate, $C_{22}H_{42}O_4$
GOX	Gaseous Oxygen
HRE	Hybrid Rocket Engine
HTPB	Hydroxyl-Terminated Polybutadiene
IPDI	Iso-Phorone Di-Isocyanate, $C_{12}H_{18}N_2O_2$
LRE	Liquid Rocket Engine
LOX	Liquid Oxygen
O/F	Oxidizer to Fuel Ratio
PB	Polybutadiene
$SEBS_{MA}$	Styrene-Ethylene-Butylene-Styrene grafted with Maleic Anhydride copolymer
SPLab	Space Propulsion Laboratory
SRM	Solid Rocket Motor
TIN	Dibutyltin Diacetate, $(CH_3CO_2)_2Sn[(CH_2)_3CH_3]_2$
TMD	Theoretical Maximum Density, kg/m^3
TOT	Thickness Over Time
VFP	Vortex Flow Pancake

SUBSCRIPTS

ave	average
b	burning
bl	boundary layer
break	breaking of the wire
c	condensed phase
cc	combustion chamber
ent	entrainment
f	fuel
fin	final
fl	flame
g	gas phase
ign	ignition
in	initial
inlet	inlet
N2	N2 side fuel grain
noz	nozzle side fuel grain

ox	oxidizer
sens	sensor
tot	total

1. INTRODUCTION

Hybrid rocket engines (HREs) are often presented as an intermediate category between liquid rocket engines (LREs) and solid rocket motors (SRMs). This approach is effective in presenting the HRE architecture, with propellants in different states of matter (Chiaverini, 2007), but may be confusing when considering applications. Several open-literature studies deal with the analysis of HREs for launch system applications (Altman et al., 2007). Thanks to their intrinsic safety, the application of HREs based on conventional fuels as hydroxyl-terminated polybutadiene (HTPB) can be definitely attractivefor this application, though large burning areas are required due to the slow solid fuel regression rate *(r_f)* of these formulations. As a consequence, multi-port grains may be implemented, with system volumetric efficiency reduction (Maisonneuve et al., 2002). When considering scenarios where the specific impulse (I_s) is the leading performance parameter, as the in-space propulsion, HREs receive a limited attention due to the role played by storable LREs (Sutton et al., 2010). Recently, the European regulation on registration, evaluation, authorisation and restriction of chemicals (REACH) has posed some questions on the future applications of N_2H_4-N_2O_4 and their derivatives (European Commission, REACH, 2007). This discloses attractive perspectives for the use of HREs in this scenario, in light of high theoretical Is and operating flexibility, both affordable at reduced costs with recpect to mature storable liquid propellants.

The combustion process of hybrid rocket engines (HREs) is driven by convective heat transfer from the flame zone to the condensed phase fuel grain, with eventual thermal radiation contributions from combustion products (i.e., soot, condensed species) (Chiaverini, 2007; Altman et al., 2007; Maisonneuve et al., 2002; Sutton et al., 2010). In conventional fuels (i.e., cured polymers as HTPB), the combustion process is ruled by condensed phase pyrolysis and fuel vapor diffusion in the boundary layer. The mass blowing from the gasifying surface implies convective heat transfer blockage, thus contributing to reduced r_f with respect to solid propellants (Chiaverini, 2007). Liquefying fuels overcome this intrinsic limitation of the conventional fuels, thanks to the droplet entrainment (Carrick et al., 1995; Karabeyoglu et al., 2002). These non-conventional fuels are characterized by the formation of a liquid layer of peculiar characteristics at the boundary between the fuel solid phase, and the oxidizer stream. While part of the melted fuel is vaporized by the heat transfer from the reaction zone to the condensed phase (as in conventional formulations), a fraction of it leaves the surface in the form of liquid droplets captured and entrained by the oxidizer stream. Being in the condensed phase, these droplets do not concur to the convective heat transfer blockage (Marxman et al., 1963; Marxman, 1967; Marxman et al., 1968; Chiaverini, 2007). As a consequence, the overall regression rate of liquefying fuels is 3-4 times the one of conventional formulations. Liquefying fuels were originally investigated by Carrick and Larson (Carrick et al., 1995). A theory of the droplet entrainment mechanism was developed by researchers of the Stanford University; results discussed in (Karabeyoglu et al., 2002) clarify that the entrainment of melted fuel droplets is promoted by low viscosity and low surface tension of the liquefied layer. Solid alkanes as commercial paraffin waxes feature these characteristics, and deserve further investigation as for their possible applications to HREs. High r_f are required to design HREs delivering high thrust levels with simple grain geometry (i.e., single port perforation). At the same time, the reduced cost of paraffin-based fuel formulations, and their thermoplastic behavior could yield to the design of in-space propulsion systems granting high operating flexibility with reduced recurring costs.

The development of HREs for in-space propulsion applications requires a focus on combustion efficiency and operating flexibility (i.e., multiple ignitons, throttleability). The oxidizer vortex injection has shown interesting results in promoting the combustion efficiency of HREs (Chiaverini, 2007). In particular, an innovative engine configuration, named vortex flow pancake (VFP) offers attractive characteriztics for the development of in-space propulsion systems (Gibbon et al., 2001; Paravan et al., 2015). In the VFP configuration, two fuel disks are set facing each other and separated by an injection ring. Oxidizer injection is performed by multiple equi-spaced tangential inlets. The combustion chamber is given by the spacing between the disks. The tangential injection of the oxidier yields the insurgence of vortex flow in the combustion chamber. This internal flow-field promotes propellant mixing during the combustion. The propellant mixtures flow out of the combustion chamber by a port in one of the fuel disks. This port connects the combustion chamber and the gas-dynamic nozzle. The system features a motor length (L) to combustion chamber diameter (D) ratio, L/D < 1. Gaseous oxygen (GOX) and nitrous oxide (N_2O) are considered in the analysis as oxidizers.

The last area covered in this paper concerns the numerical simulation of the internal flow-field of HREs, with a particular focus on the VFP engine.

Currently HREs feature a low TRL, but they offer I_s performance and operating flexibility similar to those of the (mature) storable LREs (Table 1). On the other hand, HREs offer the possibility of recurring costs and environmental impact reductions, thanks to the use of green oxidizers (as hydrogen peroxide, H_2O_2). The research strategy of SPLab is designed as a comprehensive approach encompassing the analysis of solid fuel burning behavior and the investigation of details of the engine configuration. The final aim of this approach is the disclosure of the advantages of HREs to the current and future technical and market requirements.

TABLE 1: Vacuum specific impulse ($I_{s,\,vac}$) and corresponding oxidizer to fuel ratio (O/F) for different propellant combinations (NASA CEA code, combustion chamber pressure 2.0 MPa, expansion ratio 40, shifting equilibrium, heat of formation of HTPB from (Kubota, 2007)).

Propellant/ Motor Classification	Fuel	Oxidizer	$I_{s,\,vac}$, s	O/F
HRE	HTPB	LOX[a]	351	2.40
	HTPB	N_2O[b]	313	8.25
	HTPB	H_2O_2[c]	325	6.5
Storable LRE	N_2H_4	N_2O_4	343	1.40
SRM	HTPB	AP[d]	285	5.7[e]
	HTPB + Al	AP	314	5.7[f]

Notes:

[a] Liquid O_2, cryogenic oxidizer stored at 90 K.
[b] N_2O and H_2O_2, and HAN may be implemented in monopropellant thrusters (i.e., low-thrust, attitude control).
[c] H_2O_2 (98 wt.%) + H_2O (2 wt.%).
[d] Ammonium perchlorate (NH_4ClO_4).
[e] Propellant composition: AP (85 wt.%), HTPB (15 wt.%).
[f] Propellant composition: AP (68 wt.%), Al (18 wt.%), HTPB (14 wt.%); this formulation could be critical for in-space applications (condensed combustion products at exhaust).

2. LITERATURE SURVEY

A detailed survey on HRE combustion behaviour investigations and development is reported by Chiaverini in (Chiaverini, 2007). The turbulent boundary layer combustion theory developed by Marxman and co-workers shows that in a hybrid rocket motor the solid fuel regression rate depends mainly on the overall mass flux flowing over the grain (G). The latter is the sum of the oxidizer and fuel mass fluxes (G_{ox}, and G_f respectively). The overall mass flux is a function of the axial position along the grain, $G_f(x)$. For classical central perforated configurations $r_f \sim [G_{ox} + G_f(x)]^{0.8}$. The main factor limiting the r_f of conventional fuel formulations is the convective heat transfer blockage (Marxman et al., 1963; Marxman, 1967; Marxman et al., 1968). Liquefying fuels offer attractive results in regression rate enhancement, thanks to the entrainment of melted fuel droplets (Karabeyoglu et al., 2002, Part I; Karabeyoglu et al., 2002, Part II). While attractive in terms of their ballistic performance, liquefying fuels features high system complications (cryogenic hybrids (Chiaverini, 2007)), or poor mechanical properties of the fuel grain (paraffin waxes (Chiaverini, 2007; Paravan et al., 2017)). Thus, currently, no commercial application of this innovative class of fuels is reported in the open literature. Non-conventional oxidizer injection techniques and fuel grain configurations were proposed as an alternative strategy for increased performance of HREs. The long cylindrical central perforated grains with head-end injection of the oxidizer require solid fuel loading with energetic additives to increase the r_f (Risha et al., 2007; Paravan, 2012) or the use of exotic injection implementations (i.e., Lee et al., 2005; Wilkinson et al., 2010; Ohyama et al., 2012; Hayashi et al., 2017). Studies on swirl flow injection show the possible benefits in terms of regression rate enhancement and improved combustion efficiency (Yuasa et al., 1999; Lee et al., 2005; Wilkinson et al., 2010; Ohyama et al., 2012; Shimada et al., 2017). Nevertheless, the viscous dumping of the vortex injection may reduce the effectiveness of this approach on systems with high L/D. Thus, studies on non-conventional geometries were initiated (Gibbon et al., 2001; Knuth et al., 2002; Rice et al., 2003; Hayashi et al., 2017).

The research activity on paraffin-based fuels is currently focused on two main aspects: the detailed understanding of the entrainment and of its ballistic effects, and the reinforcement of paraffin-based fuel formulations. Considering the entrainment effects on the solid fuel r_f, the initial studies of Karabeyoglu (Karabeyoglu et al., 2002) were extended in (Evans et al., 2004; Risha et al., 2007), evaluating the influence of the paraffin ballistic response in the presence of energetic additives. Nano-sized tungsten, was dispersed in a paraffin matrix and the solid fuel behavior was monitored by x-ray tomography. The achieved results showed a r_f increase of 38% with respect to the non-metallized baseline. Contributions to the evaluation of the droplet entrainment mechanism and its effects are reported in (Nagakawa et al., 2011; Kobald et al., 2015). Investigations on hypergolic propellant combinations based on HNO_3 and $LiAlH_4$ are presented in (Larson et al., 2011; DeSain et al., 2011) while a survey on the r_f effects of different additives (micron- and nano-sized aluminum, Mg-B composites and alane) is reported in (Paravan, 2012). The reinforcement of the mechanical properties of paraffin-based fuels is usually pursued by the solid wax blending with thermoplastic polymers (Kim et al., 2015; Boiocchi et al. 2015). Kim (Kim et al., 2015) investigated the effects of polyethylene (PE) addition to paraffin wax considering both mechanical and ballistic properties of the final fuels. Paraffin-based blends containing 5 to 10 wt% of PE showed augmented tensile and compressive strengths, and an increased surface tension of the melted fuel. With a PE load of 10 wt%, the tensile strength of the fuel was increased of 42.4% with respect to the non-blended paraffin. At the same time, the r_f of the PE-loaded formulation was characterized by a marked decrease with respect to the pure paraffin case, due to the increased viscosity of the melted fuel layer (Kim et al., 2015). The Space Propulsion Laboratory (SPLab) of Politecnico di Milano is active in the research on hybrid fuel ballistics (Galfetti et al., 2011; Boiocchi et al., 2015). In particular, SPLab designed and developed paraffin-based solid fuel formulations with reinforcing agents, extensively tested at lab-scale.

The VFP configuration was originally proposed by Gibbon and Haag at the Surrey Space Centre (Gibbon et al., 2001). This system features a couple of fuel grains with a vortex injection between them. The authors report combustion efficiencies of 98-99% for the VFP under oxidizer mass flow rates of ~10 kg/s. Moreover, under the investigated operating conditions, no O/F shift was encountered for the motor with this peculiar configuration.

Operating flexibility is one of the main advantages typically discussed when dealing with HREs (Altman et al., 2007). Nevertheless, only few open-literature studies deal with the investigation of the forced transient behaviour of HREs (Saraniero, 1970; Karabeyoglu, 2007; Paravan et al., 2013). Original work from Saraniero (Saraniero, 1970) showed the effects of condensed phase diffusivity on the ignition and combustion of solid fuel formulations. Some authors (Karabeyoglu, 2007; Paravan et al., 2013) analysed theoretically and experimentally the forced transient behaviour of solid fuels during throttling events and other forced transient conditions. In these investigations, the thermal lag in the solid fuel grain is typically observed to be the main limiting parameter influencing the transient behaviour.

3. INVESTIGATED FUELS AND CHARACTERIZATION

3.1 HTPB fuels

Concerning the traditional fuels, the fuel formulation considered in this study is based on HTPB-R45V. Details on the fuel formulation ingredients are reported in the Table 2. The final density of the HTPB-based fuel is 920 kg/m^3.

TABLE 2: Details on the ingredients of the tested HTPB fuel formulation. The curing level of the final fuel ([NCO]/[OH]) is 1.04.

Ingredient	Role	Properties	Mass Fraction in the HTPB Fuel
HTPB-R45V	Binder	MW: 2800 kg/kmol Density at 296 K: 901 g/cm^3 Viscosity at 296 K: 8000 kg/m s Hydroxyl functionality: 2.352	79.2
Dioctyl adipate (DOA)	Plasticizer	MW: 370.5 kg/kmol Density: 920 kg/m^3 Melting temperature: 206 K Self-ignition temperature: 668 K	13.1
Isophorone diisocyanate (IPDI)	Curing agent	MW: 229.29 kg/kmol Density: 1061 kg/m^3 Melting temperature: 213 K Self-ignition temperature: 703 K	7.7
Dibutyltin diacetate (TIN)	Curing catalyst	MW: 351.01 g/mol Density: 1.321 g/cm^3 Boiling temperature: 415 K	Added in excess, 0.05% of (HTPB + IPDI) mass

The phenomenon ruling the regression rate in HREs, using HTPB as fuel, is the polymer decomposition. A detailed understanding of this phenomenon is useful to improve the performance of HREs based on traditional fuels. The flash-pyrolysis of HTPB, performed at temperatures in the range 723 K – 882 K, with a heating rate of 600 K/s (Arisawa and Brill, 1996), points out the major chemical species produced. This study identifies the Arrhenius parameters ruling the formation of the six principal decomposition products at pressures of 2 and 11 atm. It is observed that for $dT/dt \geq 100$ K/s, $p \leq 2$ atm and $T \leq 773$ - 803 K, bulk phase reactions dominate the pyrolysis of HTPB. Desorption and formation of high MW species rule the pyrolysis at $dT/dt \geq 100$ °C/s, $p = 2$ atm and $803 \text{ K} \leq T \leq 882$ K and at $dT/dt \geq 100$ K/s, $p = 11$ atm and $T \geq 723$ K. Arisawa and Brill observe a high sensitivity of the Arrhenius parameters on the temperature, while pressure has the effect of shifting the point when the transition between the two different mechanisms occurs. They also note that for final temperatures of 723 K - 773 K a white residue equal to 10% of the original sample remains on the filament, while for temperatures between 773 K and 853 K a black, carbonaceous residue is observed. The same features on the fuel grains of the SPLab VFP after a combustion test are observed.

3.2 Paraffin-based fuels

In addition to traditional HTPB-based solid fuels, liquefying fuel formulations based on a commercial microcrystalline paraffin wax (SasolWax 0907) have recently been considered at SPLab. The selected paraffin features a congealing point in the range 355-366 K, with a desnsity of 924 kg/m^3, and an oil content < 1 wt%. Both plain and blended fuels are investigated. Blended fuels use styrene-ethylene-butylene-styrene grafted with maleic anhydride copolymer ($SEBS_{MA}$) as reinforcing agent to mitigate the issue of wax poor mechanical properties (see Table 3). All the fuel formulations are loaded with carbon black (CB), to prevent in-depth penetration of thermal radiation. A detailed analysis of the investigated material characteristics (as melting point temperature, liquid layer viscosity, and maximum strain) is reported in (Paravan et al., 2017). The Table 4 shows the fuel formulations considered in this study. For $SEBS_{MA}$-containing blends, the reinforcing polymer mass fractions range from 2.5% to 10%. The Table 4 data include an evaluation of the porosity of the samples ($\Delta\rho_{\%}$) by the percent difference between the TMD and the ρ_{Actual} of the manufactured fuel, with the former as reference. The implemented manufacturing procedure yields samples of high quality and reproducibility, as testified by the agreement between TMD and $\rho_{Actual,}$ and the relatively low data scattering of the measured fuel densities. The tested formulations feature a TMD close to the one of conventional solid fuels as cured HTPB (i.e., 920 kg/m^3). The Table 5 reports the dynamic viscosities of the investigated fuels. Further details from the pre-burning characterization of the tested paraffin-based fuels (including thermal analysis data and mechanical properties investigation, can be found in (Paravan et al., 2017)).

TABLE 3: Characteristics of the tested reinforcing agent for paraffin-based blends.

Commercial Name	ρ, kg/ m^3	$T_{melting,}$ °C
SEBS grafted with MA ($SEBS_{MA}$)	910	182-187

Both SA and $SEBS_{MA}$ are considered for the paraffin matrix reinforcement thanks to their chemical compatibility and miscibility with alkanes. The SA is a fatty acid with low melting temperature used in soap, drug and candle industries. This ingredient provides an increased rigidity of the starting paraffin,

with faint effects on the mechanical properties reinforcement. The $SEBS_{MA}$ is a commercial copolymer from Sigma-Aldrich (Sigma-Aldrich website, 2018) with a chain composed by styrene, butylene, ethylene and styrene, and grafted with MA. The MA mass content in the tested copolymer is 2 wt.%. The styrene-blocks at the extremes of the SEBS macromolecule provide the thermoplastic behavior to the material. During the manufacturing, the mixing between $SEBS_{MA}$ and wax is obtained firstly by melting a 1:1 (by mass) mixture under stirring at 393 K; when the mixture becomes homogeneous, the last part of paraffin is added. The last ingredient of the blends is CB. A good temperature control is required during the manufacturing, in order to prevent a dissociation of the MA contained in the copolymer and to avoid the partial evaporation of the (eventual) lighter paraffin wax fractions. For paraffin-based mixtures, it is generally true that the higher the temperature of the melt, the stronger the shrinkage effect of the mixture into the mold during the cooling.

4. ENTRAINMENT AND REGRESSION RATE CHARACTERIZATION IN LIQUEFYING FUEL COMPOSITIONS

The entrainment of droplets from melted paraffin-based fuels is studied in a pre-burning phase thanks to a purposely implemented facility. The entrainment visualization is performed under cold-flow (i.e., non-reacting) conditions. The high-speed video recording enables qualitative investigations on the droplets formation and entrainment process, as well as a quantitative determination of their size and of the mass entrained by the flow. The same fuel formulations are then tested in a lab-scale hybrid rocket motor to achieve a relative ballistic grading emphasizing the effects of the melt layer on the regression rate of the investigated formulations.

4.1 Entrainment Cold Flow Visualization

The experimental setup for the cold flow investigation of the liquid layer entrainment is schematically shown in Fig. 1. The core of the facility is the sample-holder, an aluminum block with a longitudinal slit aligned with the oxidizer flow mean velocity (Fig. 2). The melted paraffin-based fuel is loaded in the slit, and its temperature is controlled by an electric heater. The heater enables the control of the liquefied fuel in the temperature range 333 to 473 K. The cover shown in Fig. 1 is moved by a solenoid valve (not shown in the scheme). The cover is initially lowered, shielding the liquid paraffin during the oxidizer flow setup, so as to prevent gaseous stream/liquefied fuel interactions under non-controlled conditions. When the desired oxidizer steady flow is established, the cover is raised to expose the melt layer to the gaseous stream. In the currently investigated conditions, the oxidizer mass flux is 32 $kg/(m^2s) \leq G_{ox} \leq 45$ $kg/(m^2s)$, thus yielding v_{ox} in the range 25 to 35 m/s. The melted fuel temperature is set at 473 K to enable the relative grading of the different formulations. This value is selected because the W1 features a plateau in its viscosity for this T_{ml} (Table 5). The liquid layer instability and the droplet entrainment are captured by a high-speed camera (Photron Ultima APX) faced to the optical access of the setup (Fig. 1). Whatever particle is detached from the liquid layer surface, and moves in the oxidizer flow, is considered as an *entrained droplet* in this work. Surface waves (eventually featuring filaments protruding from the liquid layer surface) are not measured in this study. A sequence of the liquid layer instability insurgence in a pure-paraffin wax formulation is shown in Fig. 3. Recorded high-speed videos are treated before data collection to remove background noise and out-of-focus particles. Preliminary operations and droplet size measurement are performed by ImageJ software (ImageJ Software Homepage, 2018). In each video, different frames are analyzed, to grant that each droplet is counted only once. Typical acquisition frame rate is 8000 fps, while the capture window measures 13 mm in length and 3.2 mm in height. Considering the limitation in the spatial

discretization, particles with area smaller than 1000 μm^2 were not considered in the analysis (due to identification limitations, considering the background noise and the video resolution). The original image sequence is turned into grayscale and then is thresholded (Paravan et al., 2018). Final image analysis focuses on the entrained particles, after background removal and elimination of the surface waves. Entrained droplets are characterized in terms of their particle size (D_{10}, D_{32}, $D_{0.5}$) and morphology, evaluated as circularity, *Ci*, defined according to (ImageJ Software Homepage, 2018)). Typically, more than 1500 droplets are analyzed in each recorded video. An overview of the tested operating conditions for the evaluation of the entrainment under cold-flow conditions is reported in Table 6.

TABLE 4: Theoretical and actual density of the investigated formulations. Interval of confidence is presented in terms of the standard deviation of four measurements on different production batches.

Fuel Id.	Formulation	TMD, KG/M^3	P_{ACTUAL}, KG/M^3	$\Delta P_{\%}$ %(WRT TMD)
W1	SasolWax 0907 (99 wt%) + CB (1 wt.%)	929	938 ± 5	-1.0
S2.5W1	SasolWax 0907 (95.5 wt%) + $SEBS_{MA}$ (2.5 wt.%) + CB (1 wt.%)	929	918 ± 1	1.1
S05W1	SasolWax 0907 (94 wt%) + $SEBS_{MA}$ (5 wt.%) + CB (1 wt.%)	929	933 ± 1	-0.5
S10W1	SasolWax 0907 (89 wt%) + $SEBS_{MA}$ (10 wt.%) + CB (1 wt.%)	928	929 ± 1	-0.1

TABLE 5: Dynamic viscosity of the tested fuel formulations (shear rate 1000 s^{-1}). For W1, over three measurements, the confidence interval is < 0.001.

Fuel Id.	T_{ml}, K	η_f, Pa s
W1	383	0.009
	393	0.008
	403	0.006
	413	0.005
	423	0.005
S2.5W1	423	0.008 ± 0.001
S5.0W1	423	0.014 ± 0.001
S10W1	423	0.040 ± NAv.

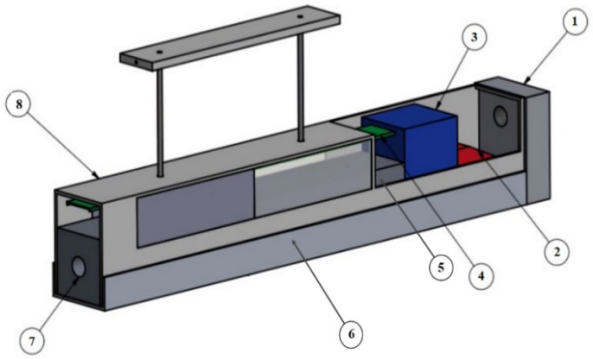

FIG. 1: Test chamber for entrainment cold-flow visualization: (1) oxidizer flow injector, (2) converging section (flow acceleration), (3) honeycomb for flow stabilization, (4) melted paraffin cover, (5) sample-holder, (6) external case, (7) heater housing, (8) windowed case.

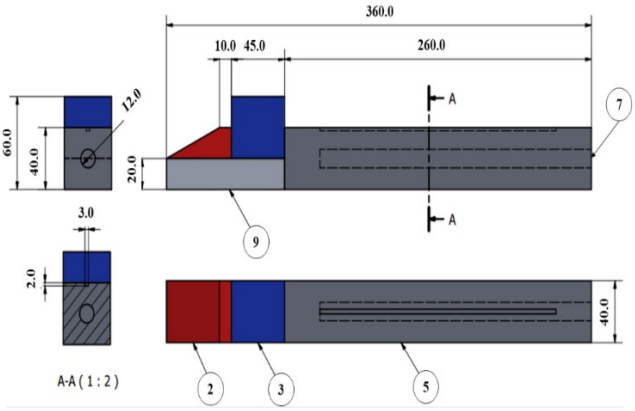

FIG. 2: Side and top views of the liquefying fuel sample holder (oxidizer flows from left to right, sizes in [*mm*]): (2) converging section, (3) honeycomb for flow stabilization, (5), sample holder, (7) heater housing, (9) supporting element.

TABLE 6: Investigated conditions and representative data entrainment cold flow visualization (average results of three runs, confidence interval defined by standard deviation), with T_{ml} = 423 K and chamber pressure p = 0.1 MPa.

Fuel Id.	G_{ox}, kg/(m^{2}s)	v_{ox}, m/s	D_{10}, µm	D_{32}, µm	$D_{0.5}$, µm
W1	32	25	115 ± 3	255 ± 25	91 ± 1
	45	35	108 ± 9	275 ± 44	82 ± 5
S5W1	45	35	91 ± 14	252 ± 79	67 ± 6

S10W1	45	35	NAv.	NAv.	NAv.

Representative results from the high-speed video recording of the cold flow visualizations are reported in Fig. 3 for W1c, and in Fig. 4 and Fig. 5 for S5W1c and S10W1c respectively.

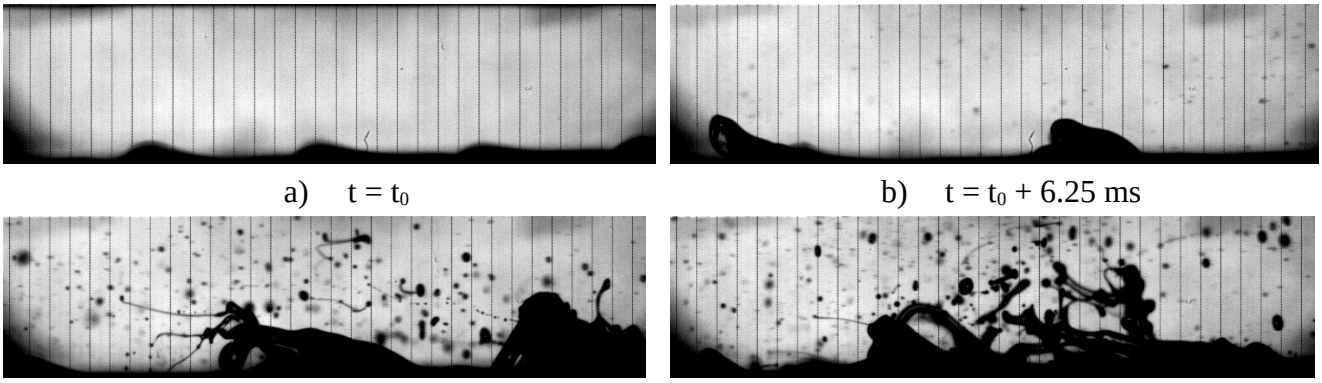

a) $t = t_0$ b) $t = t_0 + 6.25$ ms

c) $t = t_0 + 8.75$ ms d) $t = t_0 + 11.25$ ms

FIG. 3: Surface wave formation and droplet entrainment as captured by high-speed visualization. (W1, T_{ml} = 423 K, v_{ox} = 35 m/s, p = 0.1 MPa).

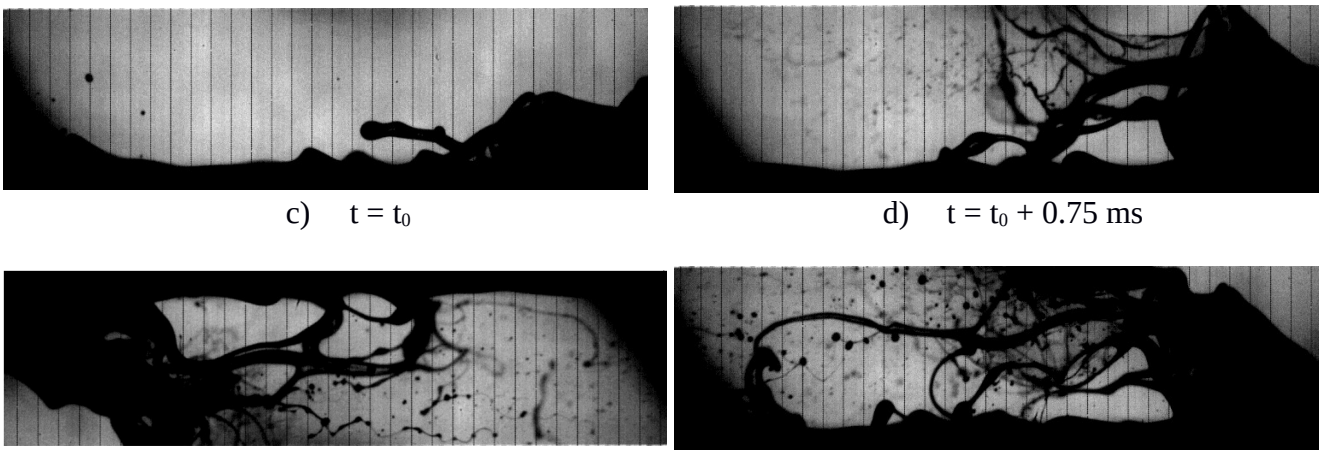

c) $t = t_0$ d) $t = t_0 + 0.75$ ms

c) $t = t_0 + 1.125$ ms d) $t = t_0 + 1.5$ ms

FIG. 4: Surface wave formation and droplet entrainment as captured by high-speed visualization (S5W1, T_{ml} = 423 K, v_{ox} = 35 m/s, p = 0.1 MPa).

Under the investigated conditions (T_{ml} = 423 K), entrainment of droplets was observed for W1c with G_{ox} > 32 kg/(m^{2}s) and for S5W1c for $G_{ox} \geq$ 45 kg/(m^{2}s). The fuel formulation loaded with 10 wt.% $SEBS_{MA}$ did not produced droplet entrainment under the tested conditions. As testified by the image sequence of Fig. 5, S10W1c interacts with the oxidizer stream creating waves eventually yielding the formation of melted fuel filaments that do not detach from the liquid layer surface. Thus, under the conditions of this study, no entrainment was recognized for the fuel formulation loaded with 10 wt.% of $SEBS_{MA}$.

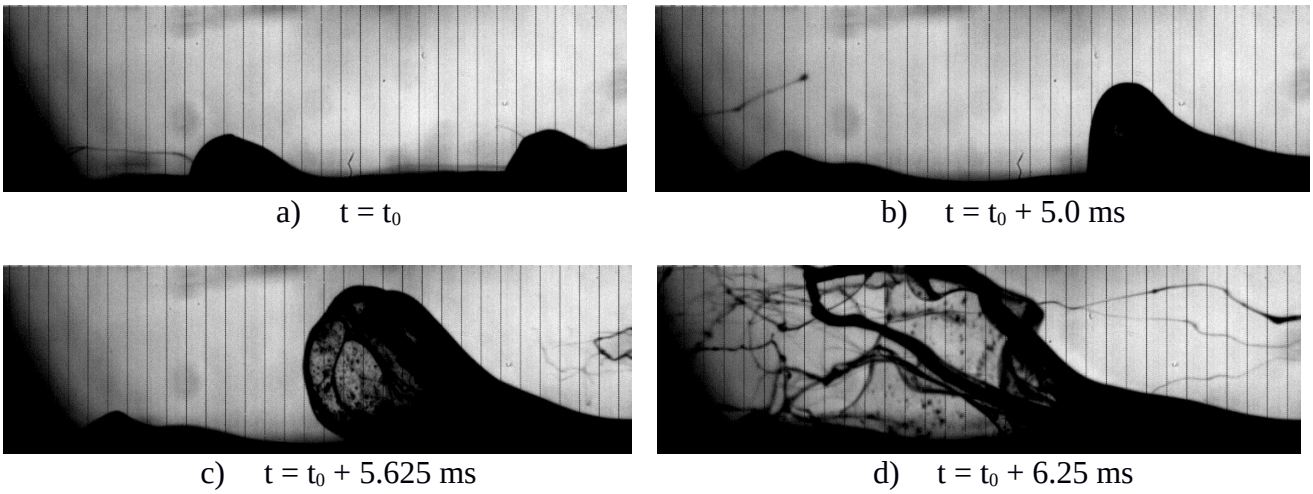

a) $t = t_0$ b) $t = t_0 + 5.0$ ms

c) $t = t_0 + 5.625$ ms d) $t = t_0 + 6.25$ ms

FIG. 5: Surface wave formation with the formation of filaments due to melt layer high viscosity, as captured by high-speed visualization (S10W1, T_{ml} = 423 K, v_{ox} = 35 m/s, p = 0.1 MPa).

4.2 Regression Rate Determination

Solid fuel regression rate is evaluated by a lab-scale HRE. The facility is designed to test cylindrical solid fuel strands with grain outer diameter of 30 mm, and single central port perforation (D_0 = 5 mm). In this work, tested specimen length is 55 mm, with solid fuel web thickness of 12.5 mm. Oxidizer is injected by swirl flow (geometric swirl number (Chiaverini, 2007), S_g = 4.75), from the sample head-end. The facility features a water-cooled brass nozzle with throat diameter of 4 mm. The grain ignition is achieved by a pyrotechnic primer charge, while combustion chamber pressure history, *p(t)*, is measured by a piezo-resistive pressure transducer. Combustion runs are performed in gaseous oxygen (GOX), with initial G_{ox} = 250 kg/m^{2}s. Gaseous N_2 is used to stop the combustion before sample burnout. Regression rate data are achieved by weight- and geometry-based based thickness over time (TOT) approaches. For the weight-based (MB) TOT, the r_f is evaluated by Δm_b, as shown in the Eq. 1

$$r_{f,MB} = \frac{\Delta m_b}{\rho_f \cdot A_{b,ave} \cdot \Delta t_b} \tag{1}$$

The mass balance of the Eq. 1, Δm_b, is the difference between the $m(t_{end})$ and $m(t_{ign})$. The average burning area for the determination of the TOT data is given by

$$A_{b,ave} = \pi \left[\frac{D(t_{end}) + D(t_{ign})}{2} \right] L_{grain} = \pi D_{b,ave} L_{grain} \tag{2}$$

The burning time ($\Delta t_b = t_{end} - t_{ign}$) is defined by the pressure trace of the run. The t_{ign} is the time in which the pressure reaches the 70% of the maximum value achieved during the run. The t_{end} is defined by the nitrogen purge inlet in the combustion chamber. The length of the grain (L_{grain}) is evaluated before the firing test (i.e., no head- or aft-end consumption during the burning is considered in the data

reduction). The average oxidizer mass flux characterizing the test is defined by the $G_{ox}(t_{ign})$, and the $G_{ox}(t_{end})$, as shown in the Eq. 3

$$G_{ox,av} = \frac{G_{ox}(t_{ign}) + G_{ox}(t_{end})}{2} = \dot{m}_{ox} \left\{ \frac{1}{\pi \left[\frac{D_{\square}^2(t_{ign})}{4} \right]} + \frac{1}{\pi \left[\frac{D_{\square}^2(t_{end})}{4} \right]} \right\} \quad (3)$$

The geometry-based TOT considers the actual diameter change of the sample during the burning, as measured after the combustion interruption. The local diameter is then directly measured by a caliper, so that the r_f is evaluated by the diameter difference (DD) as

$$r_{f,DD} = \frac{1}{\Delta t_b} \frac{D(t_{end}) - D(t_{ign})}{2} \quad (4)$$

An overview of the tests performed for r_f determination is shown in Table 7. The $G_{ox}(t_{ign})$, based on the actual (i.e., measured) diameter of the tested samples is (230 ± 13) kg/(m^{2}s). At the end of the test, the oxidizer mass flux is in the range 40 to 50 kg/(m^{2}s). For all the experimental runs, the $G_{ox,ave}$ is in the order of 120-130 kg/(m^{2}s), while the time-averaged combustion chamber pressure is in the range 0.8-1.0 MPa, thus granting similar operating conditions enabling a relative grading of the tested materials.

The fuel formulation featuring the lower viscosity, (W1, Table 5) is characterized by the fastest r_f in the dataset. In particular, for W1, with $G_{ox,ave}$ = (118.6 ± 6.5) kg/(m^{2}s), $r_{f,MB}$ = (1.70 ± 0.10) mm/s, while the TOT approach considering the (measured) diameter change yields $r_{f,DD}$ = (1.36 ± 0.08) mm/s. The difference between the MB and the DD regression rate values is mainly due to the head-end burning of the samples that is captured by the mass change method, and not by the diameter size measurement (Fig. 6). For the W1 fuel, the overall mass burning rate ($\Delta m_b/\Delta t_b$) results $3.00 \cdot 10^{-3}$ kg/s. Considering the $SEBS_{MA}$-blended fuel formulations, a decreasing r_f is observed for increasing reinforcing agent content. This is mainly due to the increased viscosity of the melt layer (Table 5). For all the formulations, the MB and the DD data enable the same relative grading. In particular, considering S2.5W1 the addition of a small amount of reinforcing polymer has no marked effects on the $r_{f,MB}$, nor on the $r_{f,DD}$. When considering the partially overlapping error bars, also the mass burning differences between the W1 and the S2.5W1 formulations appear quite limited. On the other hand, as the $SEBS_{MA}$ mass fraction increases to 5% and 10%, the regression rate decreases of 25% and 42% respectively. Under the same conditions, the mass burning rate of the fuels decreases of 28% and 47% with respect to the W1 formulation. This is probably due to the effects of the increased surface liquid layer viscosity.

TABLE 7: Space- and time-averaged r_f data from burning tests on tested liquefying fuel formulations.

Fuel Id.	$r_{f,MB}$, Eq. 1, mm/s	$r_{f,DD}$, Eq. 4, mm/s	$G_{ox,av}$, Eq. 3, kg/(m^{2}s)	$\Delta m_b/\Delta t_b$, 10^{-3} kg/s
W1	1.70 ± 0.10	1.36 ± 0.08	118.6 ± 6.5	3.00 ± 0.21
S2.5W1	1.67 ± 0.18	1.36 ± 0.01	124.5 ± 2.6	2.85 ± 0.06
S5W1	1.26 ± 0.12	1.03 ± 0.10	130.9 ± 2.2	2.15 ± 0.20
S10W1	1.01 ± 0.07	0.80 ± 0.03	119.1 ± 6.4	1.58 ± 0.04

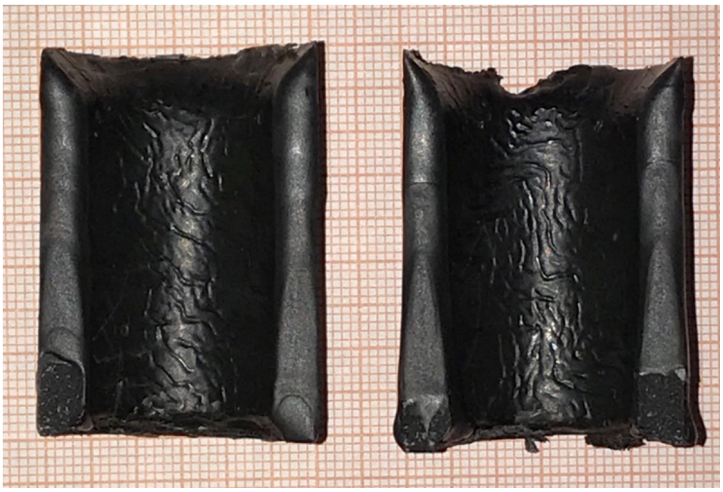

FIG. 6: Cross-sectional view of a W1 fuel grain after firing. Oxidizer flows from top to bottom. Note the effects of the head-end burning on the strand inlet section.

4.3 Discussion of the Results

In spite of the of the operating conditions differences (oxidizer mass flow rates and velocities, *p*, and temperature range), it is possible to link the fuel pre-burning characteristics (rheological behavior, cold-flow entrainment) and the burning tests. Considering a normalized regression rate ($r_{f,Norm}$) taking the $r_{f,MB}$ of W1 as the baseline, and the rheological properties of the tested fuel formulations (Table 5), a power law fitting of the achieved data yields:

$$r_{f,Norm} = 0.236 \cdot \eta_f^{-0.286}, R^2 = 0.96 \quad (5)$$

The result of Eq. (5) matches the expression proposed in (Paravan et al., 2017)

$$r_{f,Norm} = 0.979 \cdot \eta^{-0.223}, R^2 = 0.97 \quad (6)$$

The Eqs. 5-6 are developed based on different dataset considering fuel formulations based on W1 and others paraffin waxes, as well as different specimen sizes. Moreover, Eq. 6 is determined based on a time-resolved technique for the regression rate developed on a 2D radial burner enabling combustion visualization (Paravan et al., 2013; Paravan et al., 2017). These differences are a likely explaination for the differences on the pre-exponential factors of the Eqs. 5-6. On the other hand, the similarity between the power law exponents of the liquid fuel viscosity (-0.223 vs. -0.286), highlights the effect of this

parameter on the ballistic response of liquefying fuel formulations. This testifies the effect of the melt layer viscosity on the solid fuel ballistic response and the importance of a detailed analysis of the solid fuel pre-burning characteristics.

Focusing on the cold-flow visualizations of the entrainment and the fuels burning behaviors, some comments can be made: the relatively low viscosity of the W1 fuel formulation promotes the entrainment of a relatively large number of droplets from the melted fuel layer during burning. The high number of droplets seems to play a key-role for the r_f enhancement of paraffin-based fuel formulations, as can be inferred from the increased r_f performance of the unblended paraffin (Table 7). With the addition of $SEBS_{MA}$ with mass fractions $\geq 5\%$, the viscosity of the melt layer is altered with percent increases of 150% for S5W1, and 600% for S10W1. As a consequence, the number of droplets leaving the surface as observed in cold-flow tests is reduced, yielding a reduction of the measured r_f. Under the cold-flow tests experimental conditions, changes in the viscosity of the melt layer do not alter significantly the size of the droplets, while their number is reduced, with the formation of filaments protruding from the surface waves. In a reacting environment parts of these filaments may eventually interact with the flame region, with possible effects on the combustion of the fuel formulation. Under the explored experimental conditions this phenomenon seems less effective in promoting enhanced r_f than the mechanical interaction leading to the droplet formation due to the flow shear stresses, and their subsequent transport by the core flow.

5. DESIGN AND IMPLEMENTATION OF THE VFP

5.1 Logic of the VFP development

A VFP motor for the investigation of the combustion behaviour of this system was designed and implemented at the Space Propulsion Laboratory (SPLab) of Politecnico di Milano (Paravan et al., 2016; Paravan et al., 2017). Figs. 12 and 13 show a sketch and a photo, respectively, of the current implementation. SPLab studies aim at providing an understanding of the vortex combustion process and of the motor burning behaviour under quasi-steady and forced transient conditions. The target of these activities is to contribute to the implementation of this system in operating scenarios where HRE advantages may play a crucial role, as in-space propulsion (orbital manoeuvring, deorbiting) or specific missions where throttleability and multiple ignitions are the main drivers (as soft-landing, or sample return missions).

A preliminary characterization phase was performed through the internal flow-field analysis (CFD and high-speed visualizations), and firing tests (Paravan, 2016). The flow-field investigation is crucial to evaluate the effective onset of a drain type vortex in the combustion chamber, under conditions representing the whole burning envelope of the motor (i.e., from the initial fuel grain thicknesses to the combustion chamber height corresponding to burnout) (Paravan, 2016). The combustion tests are currently performed considering the combustion in gaseous O_2 (GOX) and in nitrous oxide (N_2O). As side projects in the VFP motor development, different combustion diagnostics (i.e., wire-cut and optical fiber ablation sensors) are being implemented. At the same time, evaluation of oxidizer tanks emptying dynamics and sloshing are ongoing, with a focus on N_2O as case study. The latter is selected as oxidizer considering its attractive features (i.e., simplified feed system thanks to high vapour pressure, and higher long-term stability than H_2O_2) (Heister, 2007).

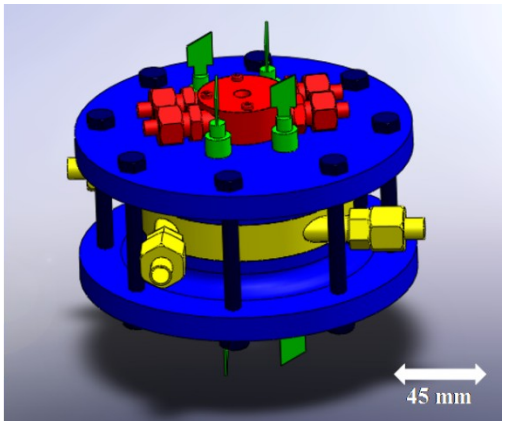

a)

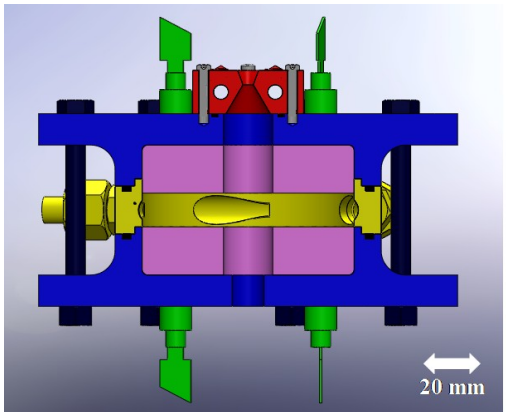

b)

FIG. 12: SPLab VFP Implementation.
(a) external and (b) cross section views: views: flanges and fuel grain holders (blue), injection ring (yellow), solid fuel grain (violet), water-cooled nozzle (red), and regression rate/fuel grain temperature sensors (green) [6].

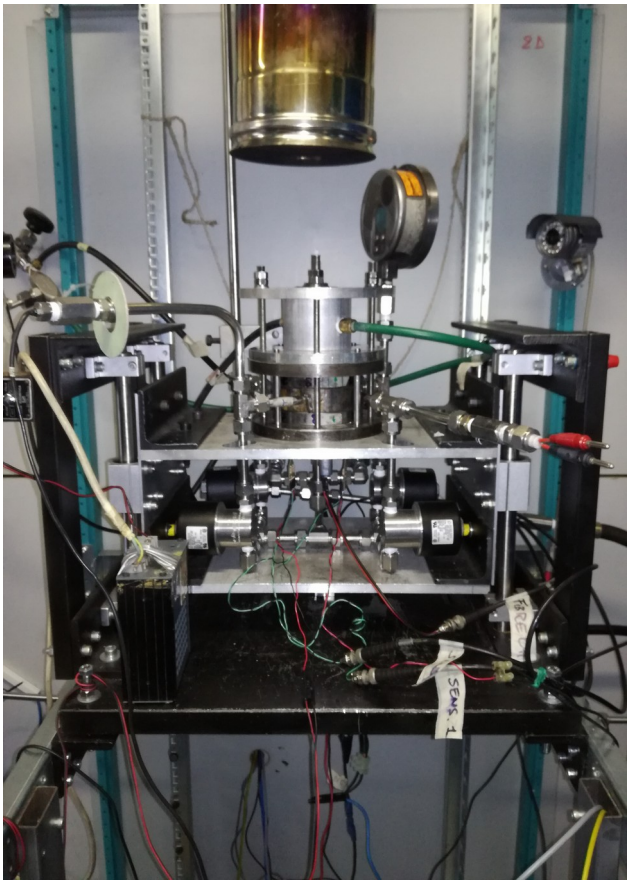

FIG 13: Details of the VFP experimental line of the SPLab. The motor is placed vertically on a moving slit (for future thrust measurement).

5.2 Structural analysis (FEA – Finite element analysis)

The current version of the VFP motor is a lab-scale implementation. The system is designed to withstand a maximum combustion chamber pressure of 6.0 MPa. The combustion chamber case, and the upper and lower flanges are realized in AISI 316 stainless steel. The nozzle is water cooled and is realized with a compact stainless steel implementation, or with a more massive copper version. In both cases, the nozzle features a throat diameter of 4 mm. The structural modelling is realized by SolidWorks®; results are reported in Fig. 14. They show that the implemented design favours operation safety over weight.

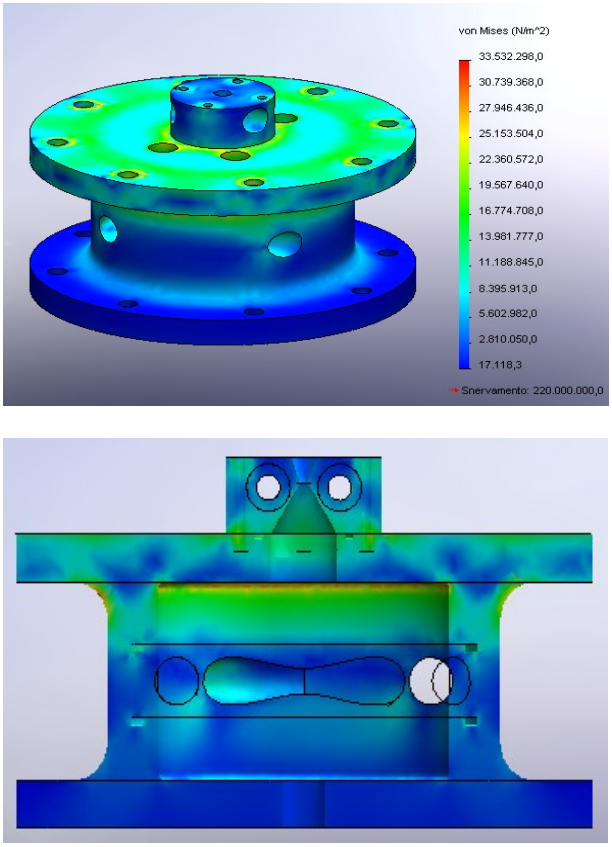

(a) (b)

FIG. 14. Finite element analysis of the SPLab heavy-weight VFP for pc = 2.0 MPa.
(a): overall view and (b): cross sectional view

5.3 Experimental setup implementation

The implemented VFP motor is remotely operated. The VFP motor is mounted on a vertical slit, enabling thrust measurement (currently not performed). The oxidizer mass flow rate is monitored by a digital flowmeter enabling live control and throttling. Each of the four inlets of the injection ring is connected to an electro-valve granting an opening/closure time of *~ 20 ms*. During a typical quasi-steady run, these actuators operate with a fifth servo-actuator that controls the N_2 purge to stop the combustion. The latter is connected to the VFP combustion chamber, and it is opposite to the nozzle-side. When the combustion is running, the N_2 purge is blocked by the electro-valve, while the oxidizer flow passes through the four inlets. A switch enables the closure of the servo-actuators serving on the oxidizer feed line, and the opening of the N_2 flow. In forced transient tests, the electro-valves may stop and restart the oxidizer mass flow. The system ignition is controlled by a propellant primer charge, in turn ignited by a hot wire. Combustion chamber pressure *(p_c)* is monitored by a piezo-resistive pressure transducer mounted on the injection terminal of one of the oxidizer injection channels. All the relevant information characterizing the test [as *$p_c(t)$* and $\dot{m}_{ox}(t)$] are synchronized by in-house developed hardware, and stored by an acquisition board (National Instruments BNC 2120).

5.4 The regression rate measurement

The regression rate of the VFP solid fuel is evaluated using two main approaches, one based on the $p_c(t)$ and a mass balance before and after the firing test, the other based on an in-house developed regression rate sensor.

5.4.1 Mass balance

The mass balance method is the less intrusive and more simple approach that can be implemented for the r_f measurement. The analysis is based on the mass change (Δm) before and after a combustion test. The regression rate is evaluated by the Eq. (7), considering the solid fuel density (ρ_f), the burning time (Δt_b) and the solid fuel grain burning surface (A_b):

$$\dot{r}_f(t) = \frac{\Delta m}{\rho_f \cdot \Delta t_b \cdot A_b} \qquad \text{for } t \in \Delta t_b \tag{7}$$

The achieved regression rate is a time- and space-averaged value. Interestingly, the peculiar VFP regression yield minor influences of the A_b changes in time, with respect to conventional grain configurations (single or multiple-port cylindrical grains). The combustion run burning time is evaluated by the $p_c(t)$. A typical pressure history in time is reported in Fig. 15. The Δt_b is conventionally defined as the time interval between the reaching of the 80% of the maximum $p_c(t)$ recorded during the test and the N_2 purge inlet (N_2 In, in Fig. 15).

The corresponding mass flux is determined considering the overall mass flow rate during the combustion run (i.e., the sum of the oxidizer and of the fuel mass flow rates), and VFP internal reference area, defined as the product of the combustion chamber radius (R_{cc}) and height (H_{cc}) (Hayashi et al., 2017). The time- and space-averaged combustion chamber height is evaluated in each combustion run considering the initial spacing between the disks and the measured r_f and Δt_b.

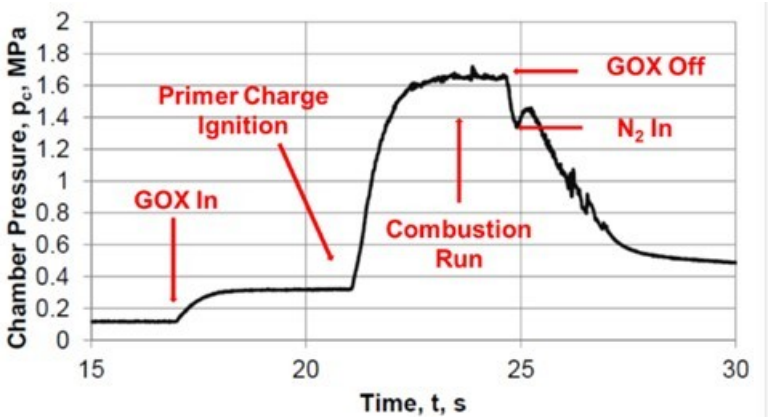

FIG. 15: Typical $p_c(t)$ of a VFP run (GOX, $\dot{m}_{ox}(t) = 10\ g/s$).

The regression rate defined by Eq. (7) is then considered for the evaluation of the time- and space-averaged O/F characterizing the considered combustion run. The O/F ratio is then considered, together with the time-averaged combustion chamber pressure, for the evaluation of the theoretical characteristic velocity (c^*) of the test. The calculation is performed by the NASA CEA code (NASA-CEA). The theoretical value is then compared to its experimental counterpart, that is evaluated

considering the actual propellant mass flow rate and nozzle throat diameter characterizing the test. Thus, the VFP combustion efficiency can be evaluated as in Eq. (8):

$$+¿\frac{c^{+¿}_{Real}}{\square}¿\,c^{\square}_{Ideal}\,c*¿\,\eta_{\square} \tag{8}$$

5.4.2 Regression rate sensor

In-house developed regression rate sensors enable the evaluation of the local *rf* evolution in time during the burning (Fig. 16). Wire-cut sensors are an intrusive, direct way of measuring the regression rate. This sensor is embedded in the fuel grain; as the fuel grain surface regresses, the wires are exposed and burned by the flame, causing a voltage step across the resistance. This method grants high accuracy and reliability and can be used both for steady state experiments and for monitoring transient events in the combustion. The sensor is based on the wire-cut scheme, and yields time-resolved r_f measurement with reduced power consumption (typically, 10 mW), high and tailorable space resolution (typically, 1 mm, though ad-hoc implementations may be easily realized). Fig. 17 shows the typical output of a VFP firing. Wire breakage is identified with a jump in the monitored tension signal. The cut of two flowing wires enables the direct r_f measurement, once the spacing between the wires and the times of the cuts are identified.

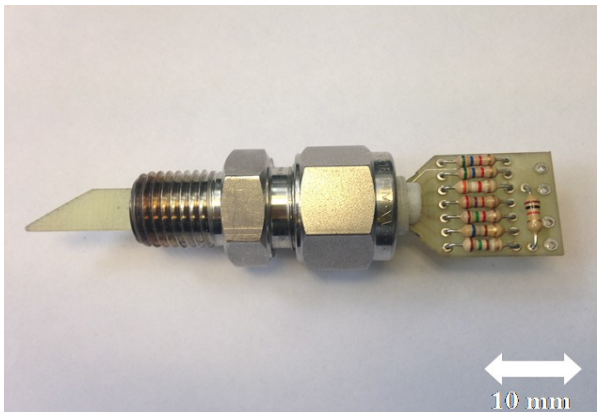

FIG. 16: Details of the SPLab wire-cut sensor.

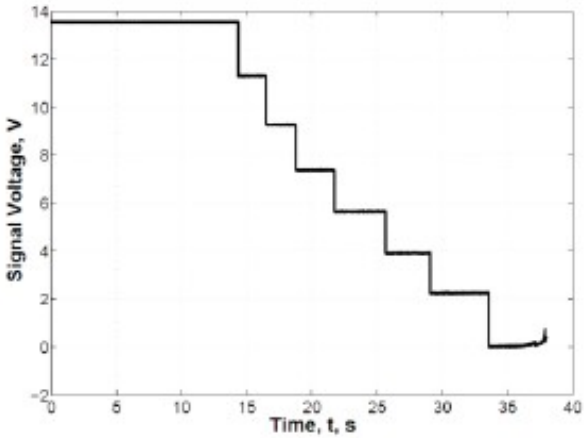

FIG. 17: Typical output signal from the in-house developed wire-cut sensor (Tadini et al., 2013).

6. EXPERIMENTAL RESULTS: QUASI-STEADY AND TRANSIENT BURNING

In this section, the experimental results are presented and discussed, starting with quasi-steady burning behaviour of the VFP followed by the evidence from a forced transient test.

6.1 Quasi-steady burning

The quasi-steady burning behaviour of the SPLab VFP is tested with GOX and N_2O oxidizers, and two different fuel formulations. The first one is a paraffin-based composition where the solid wax is reinforced by a thermoplastic copolymer $SEBS_{MA}$ (styrene-ethylene-butylene-styrene grafted with maleic anhydride) (Paravan, 2017). The paraffin-$SEBS_{MA}$ fuel contains 40 wt.% of copolymer and is labelled as S40W1 (details about the composition reported in Table 3). The second tested fuel

formulation is cured HTPB (details about the composition reported in Table 2). An overview of the performed tests, is reported in Table 9 for combustion runs in GOX, and in Fig. 18 for tests performed in N_2O (two tests, composed by 3 and 5 runs respectively).

Test No. (Fuel Id.)	Run No.	$p_c'(t)$, MPa	Δt_b, s	r_f, mm/s	$c*\eta$
1 (S40W1)	1	1.1	2.82	0.47	0.61
	2	0.5	8.19	0.39	0.68
	3	0.5	5.46	0.34	0.71
2 (S40W1)	1	0.4	4.01	0.54	NAv
3 (S40W1)	1	0.5	1.50	1.10	NAv
	2	0.3	11.6	0.44	NAv
1 (HTPB)	1	1.65	4.77	0.45	0.93
2 (HTPB)	1	1.51	4.70	0.50	0.82
3 (HTPB)	1	1.45	3.10	0.59	0.78
	2	1.26	4.21	0.36	0.77

TABLE 9: Preliminary results on VFP combustion in GOX (oxidizer mass flow rate of 10 g/s for S40W1, and 8 g/s for HTPB). Regression rate data are evaluated by a TOT technique. Operating conditions yield 1.2 ≤ O/F ≤ 2.5.

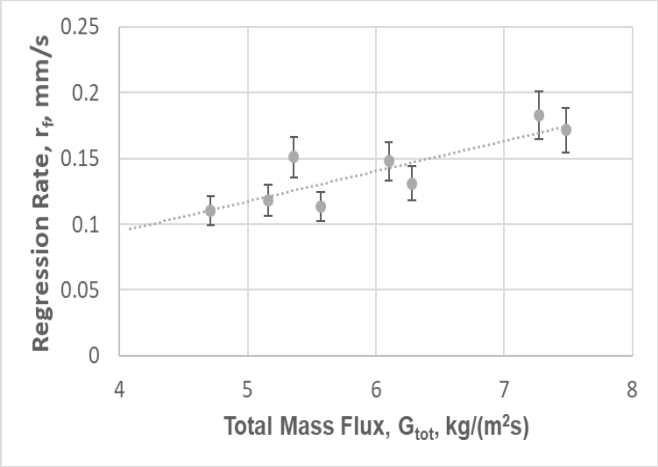

FIG. 18: Preliminary results on VFP combustion in N_2O (oxidizer mass flow rate of 5.5 g/s). Regression rate data are evaluated by a TOT technique Operating conditions yield 2.5 ≤ O/F ≤ 5.0.

S40W1 and HTPB are both tested with GOX, while only the thermosetting polymer formulation is burnt in N_2O. In GOX, the propellant-grade HTPB runs are performed with a lower $\dot{m}_{ox}$ than the S40W1 tests (8 g/s vs. 10 g/s): the achieved r_f is similar for both fuels, while the $c*\eta$ of HTPB-GOX shows higher values than the S40W1 counterpart (Table 9). The low combustion efficiency of the S40W1 is mainly due to issues with the nozzle throat thermal protection and erosion during the S40W1 runs (Paravan et al., 2016). These effects yield rough combustions and marked throat diameter changes during the experimental runs. The evaluation of the local vs. the average r_f of S40W1 runs is performed in Run 3 of Test No. 1. The comparison is obtained considering the mass balance data and comparing them with the r_f determined by the wire-cut sensors introduced in the Sec. 5.4.2. Achieved results show a good agreement between the two dataset, with a percent difference of nearly 5%. This provides a consistency check of the achieved results, and proves the uniformity of the surface regression of the VFP fuel grains (i.e., relatively flat surface with minor anisotropies). The anomalous throat erosion of the S40W1 runs is fixed in the HTPB tests. Under the investigated conditions, the combustion efficiency of HTPB-GOX is lower than in (Gibbon et al., 2001). This difference can be due to differences in the experimental setup implementation and data reduction approaches. The VFP ballistic response with both S40W1, and HTPB features a monotonic decrease of the r_f in time (that is, for

increasing H_{cc} and decreasing G_{tot}), which is not observed in (Gibbon et al., 2001). The achieved r_f (G_{tot}) is due to a reduction of the convective heat transfer as a consequence of the H_{cc} increase, and a change in intensity of the vortex flow as the fuel disks are consumed and the chamber volume increases. This effect is in agreement with the CFD analysis outputs discussed in (Paravan et al., 2016). While this phenomenon affects the regression rate behaviour, its influence on the combustion efficiency trend appears limited. The combustion efficiency is less sensitive to these operating parameters changes, since the (eventual) reduced mixing induced by the vortex structure alteration is compensated by an increase in the residence time of the reacting mixture in the combustion chamber. The relatively low $c*$¿$\eta_{\square}$values achieved during the preliminary investigation are probably due to the limited oxidizer mass flow rates used in the test campaign.

The r_f (G_{tot}) for S40W1 and HTPB is reported in the Eqs. (9) - (10) respectively:

$$\dot{r}_f\left(\dot{G}_{tot}\right) = 0.013 \cdot \dot{G}_{tot}^{1.39}, R^2 = 0.88 \quad (9)$$

$$\dot{r}_f\left(\dot{G}_{tot}\right) = 0.010 \cdot \dot{G}_{tot}^{1.50}, R^2 = 0.96 \quad (10)$$

The relatively high value of the G_{tot} in Eqs. (9) - (10) reflects different effects. For S40W1, the high G_{tot} exponent of the Eq. (9) is mainly due to the Run 1 of Test 3 (r_f *= 1.01 mm/s* for Δt_b *= 1.5 s*). This run data are strongly influenced by the ignition transient (due to the short burning time). If the considered test is removed from the analysis, the exponent of the G_{tot} in Eq. (9) turns to 0.65, with a R^2 *= 0.72*. In Eq. (10), the G_{tot} exponent > 1 is mainly due to the reduced number of tests available for HTPB, with few runs in the same test sequence ad a limited overall mass flux *[15-9 kg/(m²s)]*.

The tests performed with N_2O as the oxidizer feature the a r_f (H_{cc}) behaviour similar to the one of the GOX runs. Also combustion efficiencies show similar values, with minor influence of the combustion chamber geometry effects on this parameter. Tests performed in nitrous oxide are characterized by a reduced oxidizer mass flow rate with respect to GOX series. This may cause a reduction of the vortex intensity. The $r_f(G_{tot})$ for HTPB burning in N_2O is reported in Eq. 11:

$$\dot{r}_f\left(\dot{G}_{tot}\right) = 0.028 \cdot \dot{G}_{tot}^{0.90} \quad (11)$$

6.2 Forced-transient burning

HREs undergo forced transient conditions at motor ignition/burnout and during throttling. A preliminary result of the ballistic response of a HTPB-GOX propellant run is shown in Fig. 19. In the test, a quasi-steady burning with $\dot{m}_{ox}(t)$ *= 8 g/s* is interrupted by inlet electro-valves closure. After *3 s* of combustion, the oxidizer mass flow rate is throttled down to extinction. Consequently, the $p_c(t)$ dropped from the initial value of *1.52 MPa* to nearly *0.2 MPa*. The oxidizer mass flow rate is then restored by a throttle-up till the oxidizer mass flow rate of *8 g/s* used in the first quasi-steady leg. The electro-valve used for the oxidizer mass flow rate interruption grants a closing/opening time of *16 ms*. A waiting time of *1.95 s* follows the throttling down event. Thanks to the brief time of $\dot{m}_{ox}(t)$ interruption, the solid fuel grain is still at elevated temperature, and the hot-spots on the vaporization surface driven the motor re-ignition (Saraniero, 1970). A similar transient burning profile is implemented on conventional fuel grains, as discussed in (Paravan et al., 2013). The ballistic response of the solid fuel grain to the forced transient condition shows no marked overshoot/undershoot due to thermal lag effects in the condensed phase. The (faint) pressure oscillation observed after the throttle-up phase is, indeed, due to the flowmeter behaviour. Considering the overall burning time of the first and of the second quasi-steady

legs, the r_f evaluated in the forced transient test results *0.43 mm/s*. This, together with the overall time-averaged chamber pressure of *1.44 MPa* and the combustion time of *9.24 s* confirms that the combustion behaviour of the VFP during the forced transient is not affected by significant overshooting.

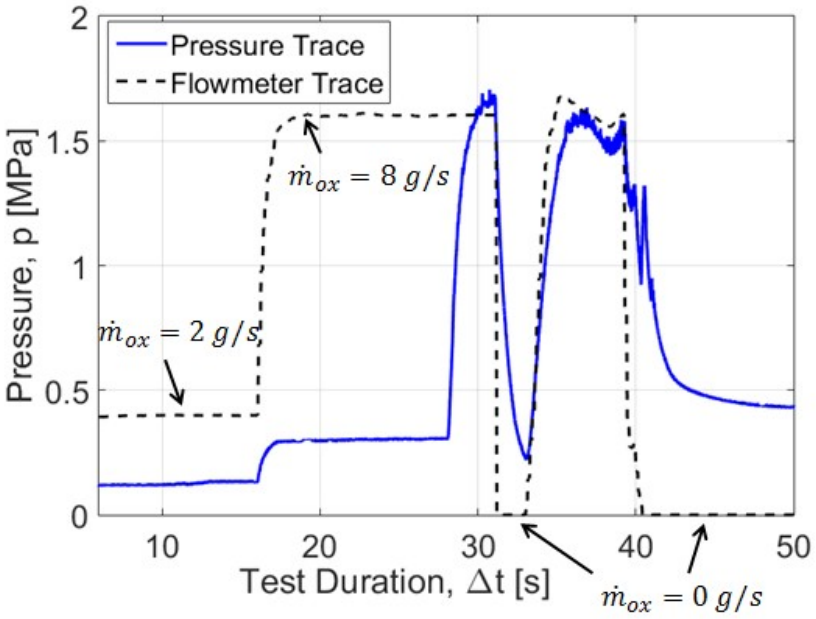

Fig. 19: Forced transient combustion by oxidizer mass flow rate extinction followed by throttling up.

6.3 Throttling and transient behavior

Throttling and re-ignition experiments cover a set of different conditions, in terms of $\dot{m}_{ox}$ and *TR*, considering several phenomena, such as the thermal lag of the fuel grains, the gas-phase kinetics, the condensed-phase kinetics and boundary layer diffusion processes (Karabeyoglu, 2007). Also the flowmeter unit characteristic time might influence the overall transient behaviour of the system. The expected order of magnitudes of the characteristic times related to such phenomena, as suggested by (Karabeyoglu, 2007), are reported in Tab. 10.

TABLE 10: Characteristic times of the phenomena contributing to the transient behaviour of generic HREs proposed by (Karabeyoglu, 2007).

τ, s	t_{fl}, s	t_c, s	t_g, s	t_{bl}, s
~10^{-1} – 1	~ 1-2	< 10^{-3}	< 10^{-3}	~ 10^{-2} – 10^{-1}

**: referred to the SPLab experimental line flowmeter*

These values for a VFP HRE must be carefully dealt with. In particular, t_{bl} is not expected to have much influence in this case, due to the peculiar geometric characteristics of the VFP. Typical values of t_c and t_g reported by Karabeyoglu (Karabeyoglu, 2007) are much smaller than τ and t_{fl}, therefore less likely to influence the overall performance of the system. In the case of the SPLab VFP

system, the transient response is likely to be ruled by the thermal lag and by the flowmeter dynamics. Characteristic times τ and t_{fl} are evaluated for all the investigated conditions.
Firing tests investigated in this study are reported in Table 11.

7. NUMERICAL RESULTS

7.1 Mesh generation

The native hexa-block mesh generator available in OpenFOAM (The OpenFOAM® Foundation, 2018) has been extended to generate a multi-block-structured grid, where the domain is divided into sub-regions, called blocks, each of which is occupied by a structured grid. Code development has been done to allow block surface morphing at the time blocks are generated. The preseted multi-block strategy shows several advantages for the specific case studied:

- it maximises the proportion of the mesh that is structured and allows the mesh to align with the main anisotropic features of the solution field and provide a nice compromise between the simplicity of structured grids and the flexibility and generality of unstructured meshes. The multiblock structured mesh also benefits of the numerical efficiencies of the structured grids;
- generation of large grids is very fast, since volume discretization is performed once mesh points and edges are already projected onto the surface.

The automated identification and creation of the blocks, the definition of the location of the mesh singularities and the overall mesh topology has been defined via a scripting procedure. The grid generation strategy is fully automatic and parametric: the main geometrical features of the pancake configuration (external and hole diameter, height, number of inlet channels) and the grid resolution are input parameters. To overcome the notorious difficulty to generate hex-block meshes, the generation strategy used in this work has been combined with the use of non-conformal mesh interfaces (Montorfano et al., 2015).
Thanks to the employed procedure, the generation of the 30 M cell grid takes less than a minute; the grid used featured 2 M cells and it was generated in about 10 seconds on a single core of a Intel-Xeon CPU E5-2650.

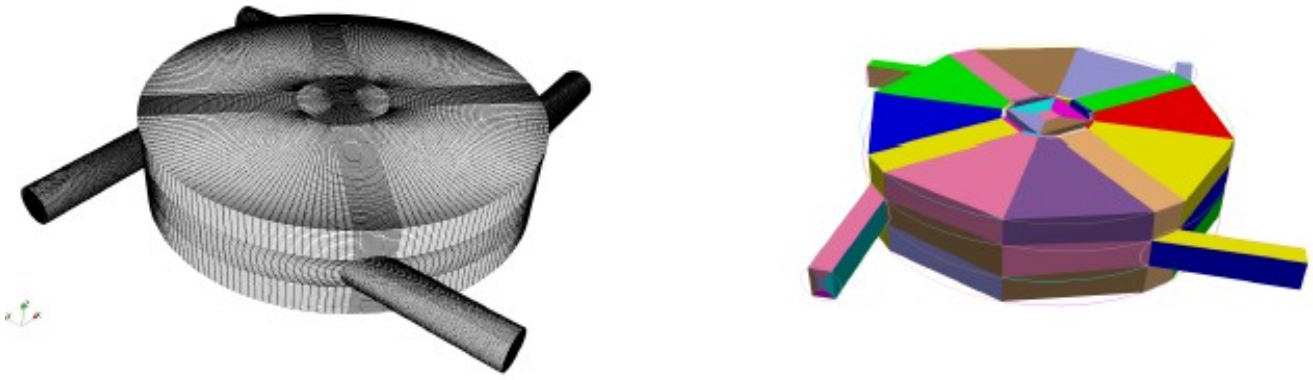

FIG. 23: Computational mesh of the hybrid rocket engine. The grid size used is about 2 M cells.

7.2 Numerical setup

The software used for the simulations is OpenFOAM®, in the development version released by the OpenFOAM Foundation (Open FOAM Foundation) with necessary extensions for hybrid RANS/LES turbulence modeling (Wu et al., 2018; Montorfano et al., 2015; Dietzel et al., 2014; Piscaglia et al., 2013) and handling of non-conformal mesh interfaces (Montorfano et al., 2015). Pressure-velocity coupling of the subsonic flow in the simulation was solved by a merged PISO-SIMPLE algorithm PIMPLE, where convergence of pressure-velocity is enforced by iterating the p-U coupling procedure within each time-step. Gaseous Oxygen is injected in the domain and its evolution is tracked. Hybrid RANS/LES modeling of turbulence is used; a description of the theory of the approach is described in the following paragraph.

7.3 Scale-adaptive Methods for Turbulence Modeling

The approach followed in this work for turbulence modeling belongs to the family of VLES methods and it has been published by the authors in (Wu et al., 2018). In contrast to LES, where the mean length scales of all unresolved turbulence are assumed proportional to the local grid spacing, VLES is usually based on statistical turbulence models where the turbulent length scale is calculated and will depend on the flow field: consequently, the rescaling procedure (Willelms, 1996) can be formulated in a dynamic and general way. The rescaling function can be activated locally in the space-time domain depending on the ratio between an estimation of the resolved turbulent length scales and the magnitude of the modeled turbulent length scales. The essence of the approach is therefore the identification of the resolvable and nonresolvable fractions of the turbulence kinetic energy (and their respective dissipation rates) and hence the identification of the unresolved portion of the Reynolds stress-tensor, which in turn influences the flow through the effects of the sub-grid motion (Willelms, 1996). There are many ways of formulating a dynamical rescaling function in a scale-resolving model: in this work, the functional form is arbitrarily defined as exponential, following the approach originally developed by Willems (Willelms, 1996) and then by Speziale (Speziale, 1998) and Fasel (Fasel et al., 2002). The function multiplies the modeled Reynolds stress tensor before solving the averaged momentum equations in order to limit the dissipation effect of the turbulence model in regions where part of the flow scales can be resolved:

$$\mu_t = g^2 \, \mu_{t,\,URANS} \tag{11}$$

Hence, the task reduces to that of multiplying the eddy viscosity calculated by an underlying URANS model by a rescaling (or damping) function g^2, which must be bounded between 0 and 1 in the inner domain, whereas it is forced to 1 on wall boundaries. It is important to note that the proposed method does not constitute a zonal approach, since the same set of equations is solved throughout the entire domain. The present approach is thought to simulate wall-bounded turbulent ows at high Reynolds numbers in complex geometries and to work with grid resolutions that are not sufficient for conventional LES to resolve smaller structures at the walls or in some specific regions of the inner domain (Piscaglia et al., 2015). Finally, the approach for turbulence modeling is strictly linked to the physics to study for the specific problem; in this sense, extensions to the code have been done to generalize the formulation of g^2 in Eq. (12) to any eddy-viscosity (compressible and incompressible) URANS model:

$$g^2 = (l_t / L_t)^{4/3} \tag{12}$$

where l_t is the minimum integral length scale that can be computed (either resolved or modeled) and L_t is the integral length scale as estimated by URANS.

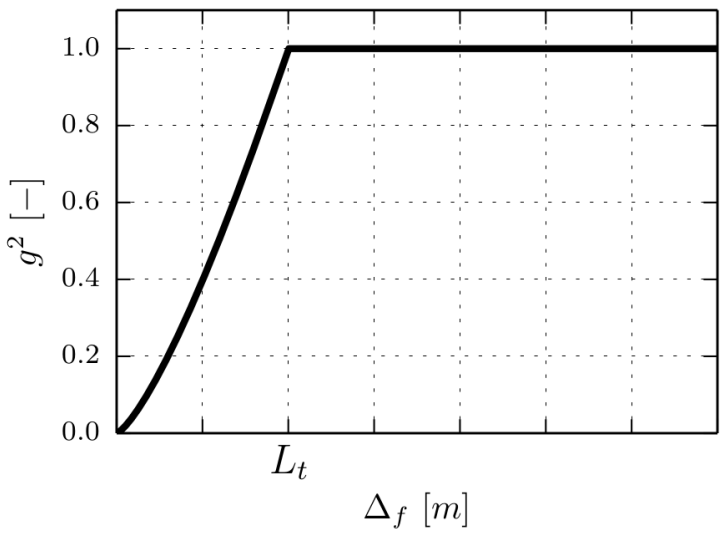

FIG. 24: The rescaling function $g^2(\Delta_f)$ is clipped to 1 as Δ_f is equal to the integral length of the modeled (URANS) scales L_t and it tends to zero in the fine grid limit.

The theory behind the definition reported in Eq. (12) is discussed in (Willems, 1996; Gyllenram et al., 2008): first, g^2 goes naturally to zero in the fine grid limit:

$$\lim_{\Delta_f \to 0} g^2 = 0 \tag{13}$$

meaning that the scale-resolving model tends to reduce the turbulent viscosity to zero when $g^2 \to 0$.It is important to note that, as it is apparent from Eqs. (12), (14) and (15), g^2 may be very low but never zero. Hence the turbulent viscosity μ_t in Eq. (11) is practically never nullified and direct numerical simulation regime is recovered only in the limit of extremely high resolutions.

7.3.1 Formulation of the rescaling function

Scale-adaptive models differ for the formulation of the rescaling function g^2 and of the filter width Δ_f, that is the upper limit of the modeled turbulent length scale and corresponds to the lower limit of the resolved turbulent length scale. In the original proposal by Speziale (Speziale, 1998), the stress damping was determined as a function of the Kolmogorov scale, this idea was pursued also in (Arunajatesan et al.; Peltier et al., 2000; Gyllenram et al., 2008) and partially in (Piscaglia et al., 2015) where l_t in the rescaling function g^2 of Eq. (2) is defined as:

$$l_t \equiv \min(\Delta_f, L_t) \tag{14}$$

In Eq. (14), Δ_f, is the estimator of the minimum resolvable length scale, determined by the time step size δt, the mesh resolution $\acute{\Delta}$ and the local flow condition:

$$\Delta_f = \alpha \max(\beta |U| \delta t, \acute{\Delta}_l) \tag{15}$$

where $\beta |U| \delta t$ is regarded as temporal resolution $\acute{\Delta}_\tau$ while $\acute{\Delta}_l$ is the spatial resolution. The coefficient β in the temporal resolution controls whether the limiting resolution has to be considered either the time-step or the mesh size. It can be demonstrated that the reciprocal of β, in fully cartesian grids, corresponds to the maximum (local) CFL number above which the time discretization may be

considered as the limiting factor of resolvable scales. The value β = 5 is used in this work, following the findings and the validation work of Wu et al., 2018.

As for the spatial resolution, $\acute{\Delta}_l$ is regarded as the spatial filter used in conventional LES, in this work it is calculated as the cube root of the local cell volume. In Eq. (15), the coefficient α represents the minimum number of grid points needed to resolve a turbulent structure. As in the very initial implementation of DLRM (Piscaglia et al., 2015), the choice of the maximum value of $\alpha = 3$ follows the choice of Gyllenram (Gyllenram et al., 2008). The calibration of α affects the operation of the rescaling function and, in turn, the performance of the hybrid model: in particular, for low values of α, the minimum length scale estimated by the the rescaling function is smaller and the turbulence model tends to resolve more scales; conversely, in authors' experience, small variations in the results of engine calculations are noticed for $\alpha > 3$.

Therefore, with the aim of limiting as much as possible the model calibration, author's choice was to assume a constant value of $\alpha = 3$.

Compared with the original definition of Δ_f in (Piscaglia et al., 2015), a few modifications have been applied on Eq. (15). Firstly, for the temporal resolution, the modified DLRM in present study considers only the local condition to relax the constraint applied in (Piscaglia et al., 2015), which is rather conservative as the maximum $|U|\ \delta t$ in the entire mesh region, instead of the local $|U|\ \delta t$, is regarded as the local temporal resolution. Secondly, due to the first modification, the coefficients before temporal and spatial resolution have to be considered separately, so new coefficient β is introduced for the temporal resolution. Finally, the implicit-LES enforcement based on Length Scale Resolution (LSR) (Brusiani et al., 2007; Piscaglia et al., 2015) has been removed: the estimation of the Kolmogorov scale in (Piscaglia et al., 2015) is based on the operation of the turbulence model which is in turn also dependent on local grid resolution. For this reason, applying at run-time a filter based on LSR would not be consistent and it could lead to an inconsistent clipping on the rescaling function g^2. This does not hold if LSR is included in the filter function when it is used a-posteriori.

The formulation of the rescaling function g^2 ensures that its derivative with respect to the estimated filter width Δ_f (as long as $\Delta_f < L_t$):

$$\partial (g^2) / \partial \Delta_f = 4/3 \, (\Delta_f / L_t)^{1/3} \tag{16}$$

tends to zero as Δ_f tends to zero:

$$\partial (g^2) / \partial \Delta_f \,|_{\Delta f \,\to\, 0} \;\to\; 0 \tag{17}$$

This shows that the eddy viscosity asymptotically approaches a constant in the fine grid limit, as long as the model equations for turbulent kinetic energy and specific dissipation rate do not explicitly depend on the local grid spacing themselves (Gyllenram et al., 2008). The rescaling function g^2 limits the contribution of modeled turbulent kinetic energy and specific dissipation rate calculated by the parent URANS model and increases the amount of the resolved portions of the flow field. In Fig. 24 an example of the rescaling function g^2 is shown: the function is clipped to 1 if Δ_f is greater than the integral length of the modeled URANS scales L_t, while the second derivative of the curve near the fine grid limit must be positive, to ensure that in that region small variations of the grid size corresponds to small variations of the resolved scales. Since the hybrid model degenerates to the URANS model wherever the local resolution becomes too coarse to support LES, the best possible URANS model for the specific engineering problem studied should be chosen. There could be an obvious risk in applying a filter width that is too small in boundary layers because, if $\Delta_f < L_t$, the formulation of the eddy viscosity would not assume the proper expected behavior $\mu_t \sim n^3$ (being n the wall-normal coordinate) (Wilcox, 2006). If the wall boundary condition for the turbulent kinetic energy $k_{wall} = 0$ were used, this

would also limit the modeled turbulent length scale and should thereby inactivate the rescaling function before the wall limit is reached. Being one of the purposes of DLRM to avoid the need of extremely high near-wall resolution, the application of a zero-flux condition is specified for the turbulence kinetic energy equation while μ_t is calculated from the wall-function of the underlying URANS model. As a consequence, grid resolution at the boundary layer and the underlying URANS model adopted must be chosen accordingly (Gyllenram et al., 2008).

7.4 Simulation of the turbulent flow in the hybrid rocket engine.

The numerical framework described has been applied to the study the vortex flow development, as reported in Fig. 25. A mass flow rate of 2.5 g/s of oxydizer has been set at the four inlet boundaries of the nominal geometry. The evolution of the turbulent flow in the combustion chamber is reported in the pictures below. A symmetric flow evolves from the outer ducts towards the center of the cylindrical geometry. The method allows to simulate the mixing process of the four jets with a good agreement, as evidenced by the comparison with the high-speed camera visualizations already published in [CITARE PRESENTAZIONE CHRISTIAN].

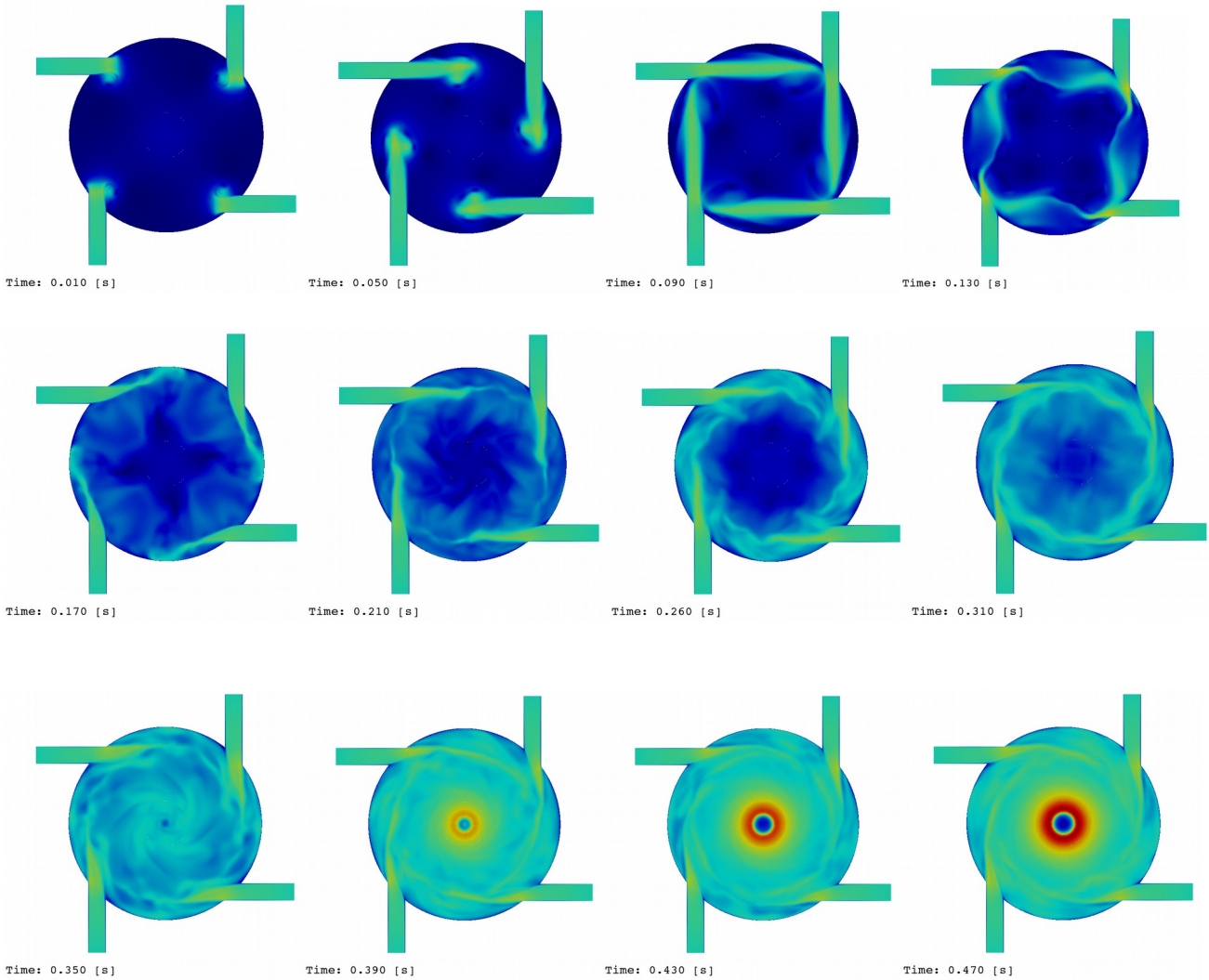

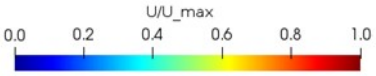

FIG. 25: Simulation of the mixing flow of four symmetric jets in the pancake engine configuration. For each outer duct an inlet mass flow rate of 2.5 g/s is set as input. The legend reports the velocity flow field, that has been normalized with respect to the maximum velocity in the computational domain.

8. CONCLUSIONS AND FUTURE DEVELOPMENTS

This paper presents a coordinated experimental and numerical investigation performed at the Space Propulsion Laboratory of Politecnico di Milano.

Traditional HTPB-based and paraffin-based fuels are investigated and characterized. The main focus is put on paraffin-based fuels, without and with reinforcing additives to improve the mechanical properties of the virgin materials. A proper selection of additives is crucial for the tuning of mechanical properties and regression rate of paraffin-based formulations. The most influential solid fuel property is the viscosity of the melted fuel. It strongly affects the regression rate and is strongly affected by the nature and amount of additives. It is shown that a decreasing viscosity of the liquid melted layer enhances the entrainment phenomenon and consequently the fuel regression rate. In particular, the reinforcement effects of SEBS-MA, a thermoplastic polymer featuring a strong reinforcing action, are investigated. Its use also implies a marked influence on the melted fuel viscosity, responsible for the entrainment phenomena of melted fuel droplets in the oxidizer stream. SEBS-MA-loaded paraffin fuels may have a good performance in terms of regression rate. A power law correlation between the solid fuel regression rate and the melt layer viscosity is identified under the investigated experimental conditions.

Experimental activities on the investigation of liquefying fuels for hybrid rocket propulsion are then presented. The first part of this section focuses on the study of the entrainment in non-reacting cold-flow conditions; in the second part the burning behavior of the tested materials is discussed. Different fuel formulations are tested, evaluating (on a relative grade) the effects of G_{ox} and melted layer viscosity on the onset and size distribution of entrained fuel droplets. The main observable difference between the fuel formulations is the shape of the entrained droplets, which suggests a possible different mechanism for their formation (i.e., from roll wave to impinging liquid). The S10W1 fuel exhibits the highest viscosity in the dataset (η_f = 0.040 Pa s). Under the investigated conditions, this compound shows surface wave formation, followed by melted fuel filaments protrusion from the surface. These filaments do not breakup into droplets and are not detached from the surface. The cold-flow investigation enables to identify the fuel formulation with the higher entrainment mass transfer, and highlights how, for the tested fuels, the droplet size is not the most relevant parameter for the evaluation of the r_f effects.

The VFP motor, thanks to the vortex combustion, promises high actual combustion efficiencies; its attractive features (compactness, easy implementation on different platforms) could yield an effective use of HRE for in-space applications spanning from orbital manoeuvring to deorbiting and soft landing. The internal flow-field of the motor is investigated by CFD analyses performed by OpenFOAM®, as described in the last part of the paper. The implemented code shows the onset of a vortex flow-field under the investigated condition. From the experimental point of view, combustion runs are performed in GOX and N_2O. With the former oxidizer, two different fuel formulations are

investigated, S40 (blended formulation of paraffin reinforced by $SEBS_{MA}$) and HTPB. The combustion of S40 shows a peculiar behaviour with low combustion efficiencies, caused by inefficient throat thermal protection. The r_f of HTPB-GOX is similar to that of S40, apart from a reduced $\dot{m}_{ox}$ (8 g/s vs. 10 g/s). Both S40 and HTPB show a decreasing regression rate behaviour for increasing combustion chamber height. This effect is not reported in previous VFP investigations available in the open literature. During the tests, multiple ignitions are achieved and no marked combustion anisotropies are identified. The HTPB combustion shows a higher combustion efficiency than S40, which is relatively independent from changes in the combustion chamber volume. Tests in HTPB-N2O show a similar trend with respect to the GOX runs. During a forced transient burning with oxidizer mass flow rate extinction followed by a throttle-up, the VFP shows an effective re-ignition triggered by the hot-spots on the grain surface. After the throttle-up, the $p_c(t)$ trace of the motor shows a regular and stable trend.

Future developments of this work will be focused on detailed analyses of the entrainment mechanism for fuels with different melt layer viscosities, and on the effects of energetic additives on the ballistic response of the designed fuels. In particular, the tailoring of the fuel characteristics should be developed focusing on the mission requirements. Further developments will also include the design of a facility for the evaluation of the melted fuel droplets under burning conditions, to integrate the cold-flow observations. In particular, the analysis of the burning conditions will enable an understanding of the interaction between the surface wave filaments and the flame region. The achieved results show promising perspectives in the implementation of a hybrid propulsion-based platform, enabling good performance and operating flexibility.

REFERENCES

Altman, D. and Holzman, A., (2007) Overview and History of Hybrid Rocket Propulsion, in: Fundamentals of Hybrid Rocket Engine Combustion and Propulsion, M.J. Chiaverini & K.K. Kuo (Eds.), AIAA Progress in Astronautics and Aeronautics, Vol. 218, Reston, Virginia. Chapter 1, pp. 1-36.

Arisawa, H., and Brill, T.B., (1996) Flash pyrolysis of hydroxyl-terminated polybutadiene (htpb): analysis and implications of the gaseous products, Combustion and Flame, vol. 106, no. 1, pp. 131–143.

Arunajatesan S., and Sinha, N.N, (2001) Unsteady RANS-LES simulations of cavity flow fields, 39th Aerospace Sciences Meeting and Exhibit, Aerospace Sciences Meetings. [Online]. Available: http://dx.doi.org/10.2514/6.2001-516.

Barton, I., (1998) Comparison of Simple- and PISO-type Algorithms for Transient Flows, Int. J. Numer. Methods Fluids, vol. 26, No. 4, pp. 459-483.

Boiocchi, M., Paravan, C., Dossi, S., Maggi, F., and Galfetti, L., (2015) Paraffin-based fuels and energetic additives for hybrid rocket propulsion", AIAA Paper 2015-4042.

Brusiani, F., Forte, C., and Bianchi, G., (2007) Assessment of a Numerical Methodology for Large Eddy Simulation of ICE Wall Bounded Non-Reactive Flows, in SAE Technical Paper 2007-01-4145. [Online]. Available: doi:10.4271/2007-01-4145.

Caravella, J.R., Heister, S.D., and Wernimont, E.J., (1998) Characterization of Fuel Regression in a Radial Flow Hybrid Rocket, Journal of Propulsion and Power, vol.14, No. 1, pp. 51-56.

Carrick, P.G., and Larson, W.C., (1995) Lab-Scale Test and Evaluation of Cryogenic Solid Hybrid Rocket Fuels, AIAA Paper 95-2948.

Chiaverini, M.J., (2007) Review of Solid-Fuel Regression Rate Behavior in classical and Nonclassical Hybrid Rocket Motors, in: Fundamentals of Hybrid Rocket Engine Combustion and Propulsion, M.J.

Chiaverini & K.K. Kuo (Eds.), AIAA Progress in Astronautics and Aeronautics, Vol. 218, Reston, Virginia. Chap. 2, pp. 37-125.

DeSain, J.D., Curtiss, T.J., Metzler, K., and Brady. B., (2011) Testing hypergolic ignition of paraffin wax/$LiAlH_4$ mixtures, AIAA Paper 2011-6636.

Dietzel, D., Messig, D., Piscaglia, F., Montorfano, A., Olenik, G., Stein, O., Kronenburg, A., Onorati, A., and Hasse, C., (2014) Evaluation of Scale Resolving Turbulence Generation Methods for Large Eddy Simulation of Turbulent Flows, Computers & Fluids, vol. 93, pp. 116-128, http://www.sciencedirect.com/science/article/pii/S0045793014000206.

European Commission, (2007) REACH (Registration, Evaluation, Authorisation and Restriction of Chemicals), website, https://ec.europa.eu/growth/sectors/chemicals/reach_en. Last visit, 01 Apr 18.

Evans, B.J., Favorito, N.A., Boyer, E., Risha, G.A., Wehrman, R.B., and Kuo, K.K., (2004) Characterization of Nano-sized Particle Enhancement of Solid Fuel Burning Rates in an X-ray Transparent Hybrid Rocket Engine, AIAA Paper 2004-3821.

Fasel, H., Seidel, J., and Wernz, S., (2002) A Methodology for Simulations of Complex Turbulent Flows, J. Fluids Eng., vol. 124, pp. 933-942.

Galfetti, L., Merotto, L., Boiocchi, M., Maggi, F., DeLuca, L.T., (2011) Ballistic and rheological characterization of paraffin-based fuels for hybrid rocket propulsion", AIAA Paper 2011-5680.

Gibbon, D. M., and Haag, Lin, S., and Kwok, C.K., (2001) Investigation of an Alternative Geometry Hybrid Rocket for Small Spacecraft Orbit Transfer, DTIC Technical Report, AD No. 393398, 2001.

Gyllenram, W., and Nilsson, H., (2008) Design and Validation of a Scale-Adaptive Filtering Technique for LRN Turbulence Modeling of Unsteady Flow, Journal of Fluids Engineering, vol. 130, p. 051401. [Online]. Available: http://dx.doi.org/10.1115/1.2911685.

Hayashi, D. and Sakurai, T., (2017) A Fundamental Study of End-Burning Swirling-Flow Hybrid Rocket Engine using Low Melting Temperature Fuels, AIAA Paper No. 2017-4138.

Heister, S. and Wernimont, E., (2007) Hydrogen Peroxide and Other Storable Oxidizers. In: Fundamentals of Hybrid Rocket Engine Combustion and Propulsion, M.J. Chiaverini & K.K. Kuo (Eds.), AIAA Progress in Astronautics and Aeronautics, Vol. 218, Reston, Virginia. Chapter 11, pp. 457-488.

ImageJ Software Homepage, (2018) https://imagej.nih.gov/ij/.

Karabeyoglu, M.A., Altman, D., and Cantwell, B.J., (2002) Combustion of Liquefying Hybrid Propellants: Part 1, General Theory, Journal of Propulsion and Power, vol.18, No. 3, pp. 610-620.

Karabeyoglu, M.A. and Cantwell, B.J., (2002) Combustion of Liquefying Hybrid Propellants: Part 2, Stability of Liquid Films, Journal of Propulsion and Power, vol.18, No. 3, pp. 621-630.

Karabeyoglu, M.A., (2007) Combustion Instability and Transient Behavior in Hybrid Rocket Motors, in: Fundamentals of Hybrid Rocket Engine Combustion and Propulsion, M.J. Chiaverini & K.K. Kuo (Eds.), AIAA Progress in Astronautics and Aeronautics, Vol. 218, Reston, Virginia. Chapter 9, pp. 351-412.

Kim, S., Moon, H., Kim, J., Cho, J., (2015) Evaluation of paraffin–polyethylene blends as novel solid fuel for hybrid rockets, Journal of Propulsion and Power, vol. 31, no. 6, pp. 1750-1760.

Knuth, W.A., Chiaverini, M.J., Sauer, J.A., and Gramer, D.J., (2002) Solid–fuel Regression Rate Behavior of Vortex Hybrid Rocket Engines, Journal of Propulsion and Power, vol.18, No. 3, pp. 600-609.

Kobald, M., Petrarolo, A., and Schlechtriem, S., (2015) Combustion visualization and characterization of liquefying hybrid rocket fuels, AIAA Paper 2015-4137.

Kubota, N., *Propellants and Explosives, Thermochemical Aspects of Combustion*, Wiley VCH, 2007.

Larson, B.D., Boyer, E., Wachs, T., Kuo, K.K., DeSain, J.D., Curtiss, T.J., and Brady, B.B., (2011) Characterization of the performance of paraffin / $LiAlH_4$ solid fuels in a hybrid rocket system, AIAA Paper 2011-5822.

Lee, C., Na, Y., and Lee, G., (2005) The Enhancement of Regression Rate of Hybrid Rocket Fuel by Helical Grain Configuration and Swirl Flow, AIAA Paper 2005-3906.

Maisonneuve, Y. and Lengellé, G., (2002) Hybrid Propulsion: Past, Present, and Future Perspectives, in: Proceedings of the 8th IWCP (International Workshop on Combustion Propulsion), L.T. DeLuca (Ed.), Pozzuoli, Naples Italy, 16-21 Jun.

Marxman, G.A., and Gilbert, M., (1963) Turbulent Boundary Layer Combustion in the Hybrid Rocket, in: 9th International Symposium on Combustion, Academic Press, Inc., New York, pp. 371-383.

Marxman, G.A., (1967) Boundary Layer Combustion in Propulsion, in: Proceedings of the 11th Symposium (International) on Combustion, The Combustion Institute, Pittsburgh, Pennsylvania, pp. 269-289.

Marxman, G.A. and Wooldridge, C.E., (1968) Research on the Combustion Mechanism of Hybrid Rockets, Advances in Tactical Rocket Propulsion, Edited by S.S. Penner, AGARD Conference Proceedings No. 1, pp. 421-477.

Montorfano, A., Piscaglia, F., and Onorati, A., (2015) An Extension of the Dynamic Mesh Handling with Topological Changes for LES of ICE in OpenFOAM, SAE Technical Paper 2015-01-0384, http://dx.doi.org/10.4271/2015-01-0384.

Nakagawa, I., and Hikone, S., (2011) Study on the regression rate of paraffin-based hybrid rocket fuels, Journal of Propulsion and Power, vol. 27, no. 6, pp. 1275-1279.

NASA, CEA: Chemical Equilibrium with Applications, http://www.grc.nasa.gov/WWW/CEAWeb/.

Ohyama, S., Aso, S., Hirata, Y., Araki, K., Ohe, K., Tani, Y., and Shimada, T., (2012) A Study of Hybrid Rocket Engine with Multi-Section Swirl Injection Method, AIAA Paper No. 2012-3905.

Paravan, C., (2012) Ballistics of Innovative Solid Fuel Formulations for Hybrid Rocket Engines, Ph.D. Dissertation, Dept. of Aerospace Science and Technology, Politecnico di Milano, Milan, Italy.

Paravan, C., Manzoni, M., Rambaldi, G., and DeLuca, L.T., (2013) Analysis of Quasi-steady and Forced Transient Burning of Hybrid Solid Fuels in a Laboratory-scale Burner by an Optical Technique, International Journal of Energetic Materials and Chemical Propulsion, vol. 12, Issue 5, pp. 385-410.

Paravan, C., Glowacki, J., Carlotti, S., Maggi, F., and Galfetti, L., (2016) Vortex Combustion in a Lab-Scale Hybrid Rocket Motor, AIAA Paper No. 2016-4562.

Paravan, C., Maggi, F., and Galfetti, L., (2017) A Critical Analysis of Paraffin-based Fuel Formulations for Hybrid Propulsion, AIAA Paper No. 2017-4830.

Paravan, C., Carlotti, S., DiCicco, M.A., Maggi, F., and Galfetti, L., (2017) Space Debris Mitigation and Remediation: Perspectives of Affordable Hybrid Rocket Propulsion, 7th European Space Agency Conference on Space Debris, Darmstadt, Germany, 18-21 Apr, Paper 898.

Paravan, C., Carlotti, S., Maggi, F., and Galfetti, L., (2017) Quasi-steady and Forced Transient Burning of a Vortex Flow Hybrid Motor, in: 7th EUCASS (European Conference on Aeronautics and Space Sciences), Milan, Italy, 3-6 Jul.

Paravan, C., Bisin, R., Carlotti, S., Maggi, F., and Galfetti, L. (2018) Diagnostics for Entrainment Characterization in Liquefying Fuel Formulations, AIAA Paper No. 2018-4663.

Peltier, L.J., Zajaczkowski, F.J., and Wyngaard, J.C., (2000) A Hybrid RANS/LES Approach to Large-Eddy Simulation of High-Reynolds-Number Wall-Bounded Turbulence, in Proceedings of the 2000 ASME Fluids Engineering Division Summer Meeting, Boston, Massachusetts.

Piscaglia, F., Montorfano, A., and Onorati, A., (2013) Development of a Non-Reecting Boundary Condition for Multidimensional Nonlinear Duct Acoustic Computation, Journal of Sound and Vibration, vol. 332, no. 4, pp. 922-935, 2013, http://dx.doi.org/10.1016/j.jsv.2012.09.030.

Piscaglia, F., Montorfano, A., Onorati, A., (2015) A Scale Adaptive Filtering Technique for Turbulence Modeling of Unsteady Flows in IC Engines, SAE Int. J. Engines, Paper n. 2015-01-0395, http://dx.doi.org/10.4271/ 2015-01-0395.

Rice, E.E., Gramer, D.J., St. Clair, C.P., and Chiaverini, M.J., (2003) Mars ISRU CO/O2 Rocket Engine Development and Testing, in: 7th NASA International Microgravity Combustion Symposium, NASA/CP—2003-212376, 2003.

Risha, G.A., Evans, B.J., Boyer, E., and Kuo, K.K., (2007) Metals, Energetic Additives and Special Binders Used in Solid Fuels for Hybrid Rockets, in: Fundamentals of Hybrid Rocket Combustion and Propulsion, M.J. Chiaverini & K.K. Kuo (Eds.), Progress in Astronautics and Aeronautics, AIAA, Reston, Virginia. Chap. 10, pp. 413–456.

Rutland, C.J., (2011) Large-eddy Simulations for Internal Combustion Engines - a Review, Int. J. Eng. Res., no. 12, pp. 421-451. [Online]. Available: http://dx.doi.org/10.1177/1468087411407248.

Saraniero, M.A., (1970) Combustion Anomalies in Stop-restart Firing of Hybrid Rocket Engines, Princetion University.

Shimada, T., Yuasa, S., Nagata, H., Aso, S., Nakagawa, I., et al., (2017) Hybrid Propulsion Technology Development in Japan for Economic Space Launch, in: Chemical Rocket Propulsion: A Comprehensive Survey of Energetic Materials, L.T. DeLuca, T. Shimada, V.P. Sinditskii & M. Calabrò (Eds.), Springer.

Sigma-Aldrich Website, (2018), http://www.sigmaaldrich.com/catalog/product/aldrich/.

Speziale, C.G., (1998) Turbulence Modeling for Time-Dependent RANS and VLES: A Review, AIAA Journal, vol. 36, pp. 173-184.

Speziale, C.G., (1998) A Combined Large-Eddy Simulation and Time-Dependent RANS Capability for High-Speed Compressible Flows, J. Sci. Comput., vol. 13(3), pp. 253-274.

Sutton, G.P. and Biblarz, O., (2010) Rocket Propulsion Elements, 9th Edition, Wiley, New York.

Tadini, P., Maggi, F., Colombo, G., Paravan, C., Boiocchi, M., and Vesa, S., (2013) Regression Rate Measurements in Lab-scale Hybrid Rockets, in: 5th EUCASS (European Conference on Aeronautics and Space Sciences), Munich, Germany, 1-5 July.

The OpenFOAM® Foundation. [Online]. Available: http://www.openfoam.org/dev.php.

Wilcox, D.C., (2006) Turbulence Modeling for CFD, La Ca~nada, CA, Ed. DCW Industries Inc.

Wilkinson, R., Hart, K., Day, R., and Coxhill, I., (2010) Proof-of-Concept Testing of a Sustained Vortex-Flow Configuration For Hybrid Rocket Motors, AIAA Paper No. 2010-6782.

Willems, W., (1996) Numerische Simulation turbulenter Scherstromungen mit einem Zwei-Skalen-Turbulenzmodell, Ph.D. dissertation, Institut fur Technische Mechanik, RWTH Aachen.

Wu, Y., Montorfano, A., Piscaglia, F., and Onorati, A., (2018) A study of the organized in-cylinder motion by a dynamic adaptive scale-resolving turbulence model, Flow, Turbulence and Combustion, vol. 100, no. 3, pp. 797-827, Dec 2018. [Online]. Available: https://doi.org/10.1007/s10494-017-9881-3.

Yuasa, S., Shimada, O., Imamura, T., Tamura, T., and Yamamoto, K. (1999). A Technique for Improving the Performance of Hybrid Rocket Engines, AIAA Paper No. 99-2322.